Solar Sail Cooperative Formation Flying Around L_2-Type Artificial Equilibrium Points

Wei Wang[(1)]*, Hexi Baoyin[(1)], Giovanni Mengali[(2)], Alessandro A. Quarta[(2)]

[(1)] *School of Aerospace Engineering, Tsinghua University, Beijing 100084, China*

[(2)] *Department of Civil and Industrial Engineering, University of Pisa, I-56122 Pisa, Italy*

Abstract

The aim of this paper is to propose a distributed control architecture for a solar sail-based formation, flying around an L_2-type artificial equilibrium point in the Sun-[Earth+Moon] circular restricted three-body problem. Two typical cases, depending on whether the formation structure is leaderless or includes a virtual leader, are investigated. In particular, the virtual leader case is further analyzed according to whether the state information of the virtual leader is available to all of the sails or to a part of the formation structure only. The protocols of the consensus-based algorithms are formulated on a general directed (unidirectional) communication topology, by exploring each available local neighbor-to-neighbor information interaction in a cooperative manner. In that case, a synchronized formation tracking may be achieved while increasing the reliability of the formation system. Illustrative examples show the effectiveness of the proposed approach in a typical mission scenario.

Keywords: solar sail formation, artificial halo orbit, cooperative control, consensus

Nomenclature

$\boldsymbol{a}$	=	propulsive acceleration vector [$\mathrm{mm/s^2}$]
$\boldsymbol{e}$	=	relative position errors [km]
$\mathcal{E}$	=	set of edges
$\mathcal{G}$	=	communication topology graph
$\mathbb{I}$	=	identity matrix
$\mathbb{L}$	=	Laplacian matrix (with entries $[l_{ij}]$)
m	=	mass, [kg]
N	=	number of solar sails
n	=	order of Fourier series
$\boldsymbol{n}$	=	sail normal vector
$\mathbb{O}$	=	zero matrix
O	=	reference frame origin
$\boldsymbol{r}$	=	position vector (with $r = \|\boldsymbol{r}\|$), [au]
s	=	solar sail
t	=	time, [days]
$\mathcal{T}$	=	rotating reference frame
u	=	reflectivity modulation ratio
$\boldsymbol{u}$	=	control input vector

*Corresponding author

Email addresses: wei_wang@mail.tsinghua.edu.cn (Wei Wang[(1)]), baoyin@tsinghua.edu.cn (Hexi Baoyin[(1)]), g.mengali@ing.unipi.it (Giovanni Mengali[(2)]), a.quarta@ing.unipi.it (Alessandro A. Quarta[(2)])

Published in Acta Astronautica, Vol. 169 April 2020, pp. 224–239. doi: https://doi.org/10.1016/j.actaastro.2019.10.028

$\mathcal{V}$	=	set of vertices
$\mathbb{W}$	=	weighted adjacency matrix (with entries $[w_{ij}]$)
x, y, z	=	components of position vector in rotating frame
$\hat{\boldsymbol{x}}$, $\hat{\boldsymbol{y}}$, $\hat{\boldsymbol{z}}$	=	unit vectors of rotating coordinate axes
$\boldsymbol{X}$	=	state vector (with $\boldsymbol{X} \triangleq [\boldsymbol{r}^{\mathrm{T}}, \dot{\boldsymbol{r}}^{\mathrm{T}}]^{\mathrm{T}}$)
β	=	lightness number
θ, ϕ	=	attitude angles, [rad]
μ	=	dimensionless mass of [Earth+Moon] system
$\boldsymbol{\rho}$	=	relative position vector with respect to nominal halo orbit, [km]
υ	=	vertex
$\boldsymbol{\Phi}$	=	state-transition matrix
$\boldsymbol{\omega}$	=	angular velocity vector (with $\omega = \|\boldsymbol{\omega}\|$), [rad/day]

Subscripts

0	=	initial value
f	=	final value
h	=	nominal halo orbit
i	=	ith solar sail
$\oplus$	=	[Earth+Moon]
$\odot$	=	Sun

Superscripts

T	=	transpose
$\cdot$	=	time derivative
$\wedge$	=	unit vector

1. Introduction

Halo orbits around collinear Lagrangian points enable a variety of advanced scientific missions, including the recent China's lunar probe Chang'e-4 [1] . In particular, continuous relay communications between Earth and Chang'e-4, which reached the south pole region on the far side of the Moon on 3 January 2019, has been obtained via the satellite Queqiao, which entered its Earth-Moon L_2 halo orbit on 15 June 2018. Periodic (or quasi-periodic) orbits around collinear Lagrangian points have attracted much attention of the scientific community due to their unique merits. For example, in the Earth-Moon system, the non-Keplerian orbits sunward of the L_1 point are useful for space weather observations [2], while orbits near the L_2 point (with a sufficient out-of-plane displacement from it) facilitate constant telecommunication between the Earth and the far side of the Moon [3, 4, 5], as in the case of Chang'e-4 mission [6]. From a heliocentric point of view, halo orbits in the vicinity of the Sun-[Earth+Moon] L_2 point naturally avoid solar eclipses (a favorable condition for cosmic microwave measurements) , while halo orbits around the L_1 point are never shadowed by the Earth or the Moon (a favorable condition for both Earth's sunlit hemisphere observation and heliophysics studies [7, 8]). The halo orbits around the Sun-[Earth+Moon] L_2 point have been proposed and studied for several scientific missions [9, 10, 11]. For example, the (past) ESA Herschel and Plank space observatories [12, 13, 14, 15], the (present) Gaia probe [16, 17, 18], and the (planned) ATHENA [19, 20] or PLATO [21] spacecraft.

The intrinsic instability of halo orbits around collinear Lagrangian points requires effective methods for station keeping [22] which, usually, necessitate a typical ΔV budget of a few m/s/year or a (very) low propulsive acceleration, when a continuous-thrust propulsion system is considered in the mission design. The low level of necessary thrust, together with the typical requirement of a long mission time to collect a meaningful set of scientific data, make the generation of halo orbits around collinear Lagrangian point an interesting option for a solar sail-based spacecraft [23, 24, 25, 26, 27], which exploits the natural solar radiation pressure to generate a continuous thrust using the interaction of solar photons with a large reflecting

surface, without any propellant consumption. After the striking success of the pioneering Japanese mission IKAROS [28, 29], solar sailing is now considered a promising alternative to conventional (either chemical or electric) propulsion systems [30, 31].

In addition, the use of a propellantless propulsion system, such as the solar sail or the electric solar wind sail [32, 33], allows the collinear equilibrium point to be suitably displaced, so as to obtain a family of Artificial Equilibrium points (AEPs), whose distance from the Earth may be varied within some limits by properly selecting the spacecraft propulsive acceleration [5, 34]. In this context, the concept of solar sail formation flying has been suggested as an effective means for improving the observation capability (in terms of field of view and resolution) and reducing the overall system cost [35, 36, 37, 38]. In fact, the payload mass of each spacecraft may be reduced by disaggregating the functional modules among different sails, with each sail conveying the indispensable mass only. Such a mass reduction results in a significant increase of propulsive acceleration, which in turn mitigates the demanding requirement of guaranteeing a very high area to mass ratio in some future scientific missions. In addition, a formation enables multiple solar sails to operate within a limited region to fulfill complex spaceborne tasks, which would be otherwise infeasible for a single monolithic sail. By exploiting a task distribution among smaller, less-expensive spacecraft, the sails in formation are able to interact with each other and operate in a cooperative way, so that the overall system flexibility may be significantly enhanced [39].

The study of spacecraft formation flight is usually addressed by means of a leader-follower formation architecture [36, 38, 40], in which the leader moves along a predefined (nominal) trajectory, and the followers track the leader with some given (possibly time-varying) offset. In that case, the feature of the formation system is defined by specifying the behavior of the leader alone, while the information flow goes from the leader to the followers, without any feedback [41, 42, 43]. Such a topological structure introduces an inherent vulnerability, because the leader is a single point of failure for the whole system so that, when the follower is subject to strong perturbations, the formation may hardly be maintained. In most studies on the maintenance of a spacecraft formation, the leader state is assumed to be available to each follower, even though this is usually unrealistic due to small communication bandwidths and range limitations. In practice, only a part of the formation has usually access to the state of the reference point and those spacecraft may have not a directed path to all of the other formation agents.

Recently, the design of solar sail [40] (or electric solar wind sail [44, 45]) formation flying around displaced orbits has been analyzed using a consensus-based control law, which uses a coordinated cooperative control algorithm to guarantee a given formation geometry [46, 47, 48]. The aim of this paper is to extend the concept of consensus-based control to a solar sail formation structure flying around an L_2-type AEP in the Sun-[Earth+Moon] circular restricted three-body problem. In particular, two different cases are investigated, depending on whether the formation structure is leaderless or it includes a virtual leader. In the latter case the information of the virtual leader state may be available to all of the sails or to a part of the formation structure only. The protocols of the consensus-based algorithms are formulated on a general directed (unidirectional) communication topology, by exploring every available local neighbor-to-neighbor information interactions in a cooperative manner. In that case, a synchronized formation tracking can be achieved while the reliability of the formation system is strengthened.

This paper is organized as follows. Section 2 illustrates the procedure for generating an L_2-type AEP in the Sun-[Earth+Moon] circular restricted three-body problem using a solar sail-based spacecraft. Section 3 presents an approximate analytical solution to the nominal orbit via Fourier series expansions, while Sections 4 and 5 develop the formation design, and the solar sail coordinated control strategies by accommodating information interactions among the spacecraft to account both for the leaderless case, and the virtual-leader case. The proposed method is then validated in Section 6 by numerical simulations. Finally, some concluding remarks are given in Section 7.

2. Generation of L_2-type artificial equilibrium points

Consider a flat, perfectly reflecting [49, 34], solar sail s with a total reflective area A_s, which moves within the Sun-[Earth+Moon] system. The solar sail is equipped with a reflectivity control device, which comprises a number of sufficiently small Electrochromic Material Panels (EMPs) of total area A_p, whose optical coefficients may be changed with the application of a suitable electric voltage. In particular, let the area covered with the switched-off EMPs be denoted by A_{off} [40]; see Fig. 1.

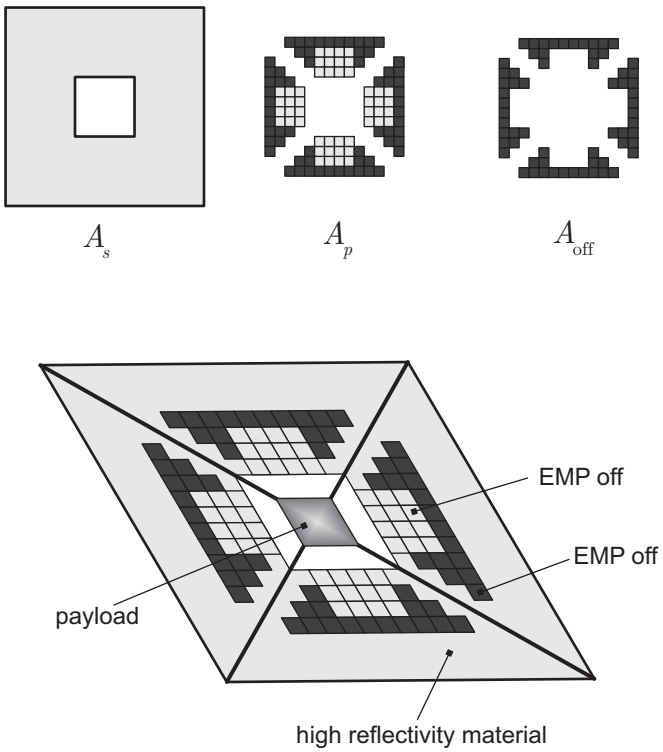

Figure 1: Conceptual scheme of a solar sail with Electrochromic Material Panels.

According to the simplified mathematical model discussed by Mu et al. [50], each EMP acts as a perfectly absorbing (or perfectly reflecting) medium in a power-off (or power-on) mode. Therefore, the magnitude of the sail propulsive acceleration can be modulated, within a suitable range, by selecting the working state of the EMPs between the high reflectivity mode (power-on), and the low reflectivity mode (power-off). Taking into account the results of Ref. [50], the solar sail propulsive acceleration vector $\boldsymbol{a}$ can be written as

$$\boldsymbol{a} = \frac{\beta\, G\, m_{\odot}}{2\, r_{\odot s}^2}\ (\hat{\boldsymbol{r}}_{\odot s} \cdot \hat{\boldsymbol{n}})\ [u\, \hat{\boldsymbol{r}}_{\odot s} + 2\ (1-u)\ (\hat{\boldsymbol{r}}_{\odot s} \cdot \hat{\boldsymbol{n}})\ \hat{\boldsymbol{n}}] \tag{1}$$

where G is the universal gravitational constant, $m_{\odot}$ is the Sun's mass, $\boldsymbol{r}_{\odot s}$ is the Sun-sail vector (with $r_{\odot s} \triangleq \|\boldsymbol{r}_{\odot s}\|$ and $\hat{\boldsymbol{r}}_{\odot s} \triangleq \boldsymbol{r}_{\odot s}/r_{\odot s}$), $\hat{\boldsymbol{n}}$ is the unit vector normal to the sail plane in the direction opposite to the Sun, and β is the sail lightness number [34], defined as the ratio of the maximum propulsive acceleration magnitude of a perfectly reflecting sail to the (local) solar gravitational acceleration. In Eq. (3), $u \triangleq A_{\text{off}}/A_s$ is the reflectivity modulation ratio which, in this simplified model, is assumed to range with continuity between 0 (when all of EMPs are in power-on mode) and $u_{\max} \triangleq A_p/A_s \leq 1$ (when all of EMPs are in power-off mode). Accordingly, the control variables are the reflectivity modulation ratio u, and the normal unit vector $\hat{\boldsymbol{n}}$. Note that in the special case of $u = 0$, Eq. (1) reduces to the formula describing an ideal solar sail [49, 34] (in which all of the incoming photons are specularly reflected), whereas if $u = u_{\max} = 1$, the solar sail acts as a flat black-body of area A_s (all of the incoming photons are absorbed).

Assuming that the [Earth+Moon] system, of mass $m_{\oplus}$, covers a circular orbit around the Sun with radius $r_{\oplus} \triangleq 1\,\text{au}$, the motion of the (massless) solar sail-based spacecraft can be described in a synodic reference frame $\mathcal{T}\,(O; \hat{\boldsymbol{x}}, \hat{\boldsymbol{y}}, \hat{\boldsymbol{z}})$, with origin at the center-of-mass O of the Sun-[Earth+Moon] system, which rotates synchronously with the revolution of the [Earth+Moon] around the Sun with an angular velocity $\boldsymbol{\omega}$. In this frame, the unit vector $\hat{\boldsymbol{x}}$ points towards the [Earth+Moon] center-of-mass, $\hat{\boldsymbol{z}}$ lies in the direction of the angular velocity vector $\boldsymbol{\omega}$, while the plane $(\hat{\boldsymbol{x}}, \hat{\boldsymbol{y}})$ coincides with the ecliptic plane; see Fig. 2.

The components of the sail normal unit vector $\hat{\boldsymbol{n}}$ can be expressed, as a function of two attitude angles

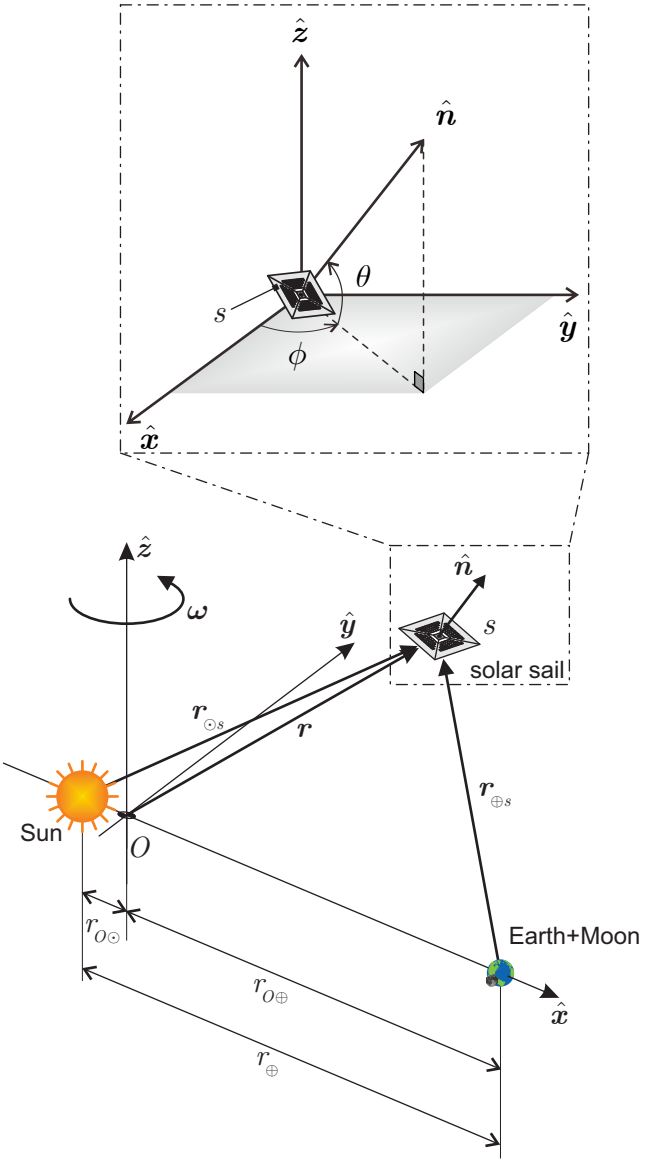

Figure 2: Synodic reference frame and solar sail thrust vector angles.

$\{\theta,\, \phi\}$, as

$$[\hat{\boldsymbol{n}}]_{\mathcal{T}} = [\cos\,\theta\,\cos\,\phi,\ \cos\,\theta\,\sin\,\phi,\ \sin\,\theta]^{\mathrm{T}} \tag{2}$$

where $\theta \in [-\pi/2,\, \pi/2]\,\mathrm{rad}$ is the angle between the direction of $\hat{\boldsymbol{n}}$ and the $(\hat{\boldsymbol{x}}, \hat{\boldsymbol{y}})$ plane, while $\phi \in [-\pi/2,\, \pi/2]\,\mathrm{rad}$ is the angle (measured counterclockwise) between the direction of $\hat{\boldsymbol{x}}$ and the projection of $\hat{\boldsymbol{n}}$ onto $(\hat{\boldsymbol{x}}, \hat{\boldsymbol{y}})$; see Fig. 2.

For convenience, a dimensionless set of units is now introduced, such that the total mass of the primaries $(m_{\odot} + m_{\oplus})$, the Sun-[Earth+Moon] reference distance $(r_{\oplus})$, and the universal gravitation constant (G) are all unitary. Accordingly, the rotational period of the synodic frame is $T = 2\,\pi/\omega \equiv 2\,\pi$, the O-Sun distance is $r_{O\odot} = \mu\, r_{\oplus} \equiv \mu$, the O-[Earth+Moon] distance is $r_{O\oplus} = (1-\mu)\, r_{\oplus} \equiv (1-\mu)$, where $\mu \triangleq m_{\oplus}/(m_{\oplus}+m_{\odot}) = 3.05425 \times 10^{-6}$ is the dimensionless mass of the [Earth+Moon] system. In particular, since the Sun's mass can be written in a dimensionless form as $m_{\odot} = (1-\mu)\,(m_{\odot} + m_{\oplus}) \equiv (1-\mu)$, the solar sail propulsive

acceleration vector $\boldsymbol{a}$, given by Eq. (1), becomes

$$\boldsymbol{a} = \frac{\beta\,(1-\mu)}{2\,r_{\odot s}^2}\,(\hat{\boldsymbol{r}}_{\odot s}\cdot\hat{\boldsymbol{n}})\,[u\,\hat{\boldsymbol{r}}_{\odot s} + 2\,(1-u)\,(\hat{\boldsymbol{r}}_{\odot s}\cdot\hat{\boldsymbol{n}})\,\hat{\boldsymbol{n}}] \tag{3}$$

Therefore, the solar sail (dimensionless) equation of motion is

$$\ddot{\boldsymbol{r}} + 2\,\boldsymbol{\omega}\times\dot{\boldsymbol{r}} = \frac{\partial\,\Omega}{\partial\,\boldsymbol{r}} + \boldsymbol{a} \tag{4}$$

where $\boldsymbol{r}$ is the O-sail position vector, $\boldsymbol{a}$ is given by Eq. (3), Ω is the effective potential function, while

$$[\boldsymbol{\omega}]_{\mathcal{T}} = [0,\,0,\,1]^{\mathrm{T}} \tag{5}$$

is the angular velocity vector and

$$[\boldsymbol{r}]_{\mathcal{T}} = [x,\,y,\,z]^{\mathrm{T}} \tag{6}$$

is the sail position vector. With the aid of Fig. 2, the potential function Ω can be written as

$$\Omega \triangleq \frac{x^2+y^2}{2} + \frac{1-\mu}{r_{\odot s}} + \frac{\mu}{r_{\oplus s}} \tag{7}$$

where the Sun-sail distance $r_{\odot s}$ and the [Earth+Moon]-sail distance $r_{\oplus s} \triangleq \|\boldsymbol{r}_{\oplus s}\|$ are given by

$$r_{\odot s} = \sqrt{(x+\mu)^2 + y^2 + z^2} \tag{8}$$

$$r_{\oplus s} = \sqrt{(x+\mu-1)^2 + y^2 + z^2} \tag{9}$$

In the simple case of $\boldsymbol{a} = 0$, Eq. (4) presents five equilibrium points, that is, the five classical equilibrium points $\{L_1, L_2, L_3, L_4, L_5\}$ of the circular restricted three-body problem, among which L_2 is the (unstable) collinear point along the Sun-[Earth+Moon] line past the [Earth+Moon] system. Assuming $\hat{\boldsymbol{n}} = \hat{\boldsymbol{r}}_{\odot s} = \hat{\boldsymbol{x}}$, a suitable value of the sail lightness number β allows the L_2 equilibrium point to be displaced along the $\hat{\boldsymbol{x}}$-axis of the synodic reference frame $\mathcal{T}$, such as to obtain a sort of L_2-type artificial equilibrium point (AEP) [5]. In other terms, when the propulsive acceleration balances both the celestial body gravitational pull and the centrifugal force along the Sun-[Earth+Moon] line, a new family of collinear AEPs are generated.

Bearing in mind Eq. (3), when $\hat{\boldsymbol{n}} = \hat{\boldsymbol{x}}$ and $\boldsymbol{r}_{\odot s} = (x+\mu)\,\hat{\boldsymbol{x}}$, the dimensionless propulsive acceleration vector becomes

$$\boldsymbol{a} = \frac{\beta\,(1-\mu)\,(2-u)}{2\,(x+\mu)^2}\,\hat{\boldsymbol{x}} \tag{10}$$

whereas the dimensionless potential function of Eq. (7) reduces to

$$\Omega = \frac{x^2}{2} + \frac{1-\mu}{x+\mu} + \frac{\mu}{|x+\mu-1|} \tag{11}$$

Therefore, the position $x = x_{\mathrm{AEP}}$ of the L_2-type AEP along the $\hat{\boldsymbol{x}}$-axis is obtained by enforcing the conditions

$$\dot{\boldsymbol{r}} = 0, \qquad \ddot{\boldsymbol{r}} = 0, \qquad \boldsymbol{r} = x_{\mathrm{AEP}}\,\hat{\boldsymbol{x}} \tag{12}$$

with $x_{\mathrm{AEP}} > (1-\mu)$. Substituting Eq. (11) into Eq. (4), the result is a single scalar equation

$$x_{\mathrm{AEP}} - \frac{(1-\mu)\,[1-\beta\,(1-u/2)]}{(x_{\mathrm{AEP}}+\mu)^2} - \frac{\mu}{(x_{\mathrm{AEP}}+\mu-1)^2} = 0 \tag{13}$$

whose solution gives the position of the L_2-type AEP along the $\hat{\boldsymbol{x}}$-axis.

For a given value of sail lightness number β and reflectivity modulation ratio u, the location of the AEP requires the determination of the root x_{AEP} of Eq. (13), which can be obtained using standard numerical algorithms. For example, when $u = 0.4$ and $\beta = 0.01$, Eq. (13) gives $x_{\mathrm{AEP}} \simeq 1.009$. On the other hand, for a given value of $x_{\mathrm{AEP}} > (1-\mu)$ and u, the required sail lightness number can be obtained from Eq. (13) as

$$\beta = \frac{(x_{\mathrm{AEP}}+\mu)^2\,\left[(1-\mu)/(x_{\mathrm{AEP}}+\mu)^2 + \mu/(\mu-1+x_{\mathrm{AEP}})^2 - x_{\mathrm{AEP}}\right]}{(1-u/2)\,(1-\mu)} \tag{14}$$

The function $\beta = \beta\,(x_{\mathrm{AEP}}, u)$ of Eq. (14) is illustrated in Fig. 3 for $u = \{0,\,0.4,\,1\}$. Note that, as expected, the condition $\beta = 0$ gives the position, along the $\hat{\boldsymbol{x}}$-axis, of the classical L_2 Lagrangian point.

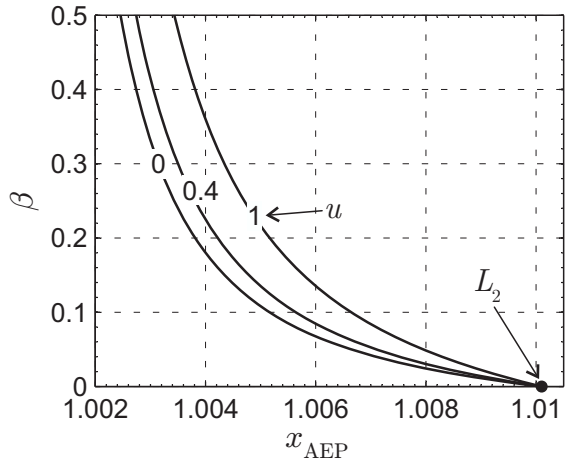

Figure 3: Required sail lightness number as a function of x_{AEP} and u; see Eq. (14).

3. Nominal trajectory selection

The reference halo orbit around the L_2-type AEP is here designated as the nominal trajectory. Nevertheless, other types of periodic or quasi-periodic orbits (e.g. Lissajous orbits) may also be chosen as the nominal trajectory, depending on the specific scientific mission requirements. In general, the properties of the dynamical system modeled by Eqs. (3)–(9) are highly dependent on the characteristics of the solar sail propulsive acceleration vector $\boldsymbol{a}$, that is, on u and on the components of the normal unit vector $\hat{\boldsymbol{n}}$; see Eq. (3).

According to Refs. [24, 51], there exists a large family of halo orbits when the sail attitude is maintained fixed in the rotating reference frame $\mathcal{T}$. In the following analysis, the nominal trajectory will be obtained under the condition $\hat{\boldsymbol{n}} \equiv \hat{\boldsymbol{r}}_{\odot s}$, that is, with the assumption that the solar sail normal vector always lies along the Sun-sail line. This happens in a Sun-facing condition, which can be maintained in a passive way by shaping the sail structure with a slightly conical form (with its apex directed sunward) [52, 53]. A Sun-facing condition can also be obtained using a Sun-pointing smart dust [54, 55, 56, 57], that is, a millimeter-scale solar sail [58] whose external surface is covered by an electrochromic reflective film. Accordingly, Eqs. (3)–(9) give

$$\ddot{x} - 2\,\dot{y} - x = -\frac{(1-\mu)\,[1-\beta\,(1-u/2)]\,(x+\mu)}{\left[(x+\mu)^2+y^2+z^2\right]^{3/2}} - \frac{\mu\,(x+\mu-1)}{\left[(x+\mu-1)^2+y^2+z^2\right]^{3/2}} \tag{15}$$

$$\ddot{y} + 2\,\dot{x} - y = -\frac{(1-\mu)\,[1-\beta\,(1-u/2)]\,y}{\left[(x+\mu)^2+y^2+z^2\right]^{3/2}} - \frac{\mu\,y}{\left[(x+\mu-1)^2+y^2+z^2\right]^{3/2}} \tag{16}$$

$$\ddot{z} = -\frac{(1-\mu)\,[1-\beta\,(1-u/2)]\,z}{\left[(x+\mu)^2+y^2+z^2\right]^{3/2}} - \frac{\mu\,z}{\left[(x+\mu-1)^2+y^2+z^2\right]^{3/2}} \tag{17}$$

The linearized form of Eqs. (15)–(17) [59], or the third-order approximation obtained with the aid of Lindstedt-Poincaré perturbation method, is usually used to identify the artificial halo orbits in the neighborhood of the L_2-type AEP point [24, 60]. However, in both cases the obtained solution gives rise to a remarkable deviation from the nominal trajectory when the (dimensionless) propagation time exceeds about one half period ($T/2 = \pi$). For this reason, an alternative approach is advisable. In this context, the differential correction method [26, 61, 62] is firstly adopted to identify the artificial halo orbit around the designed L_2-type AEP point, whose position is obtained with a given value of the pair $\{\beta,\, u\}$. For example,

the families of halo orbits around L_2-type AEPs with $u = 0.4$ and $\beta = \{0,\ 0.005,\ 0.01,\ 0.015\}$ are shown in Fig. 4.

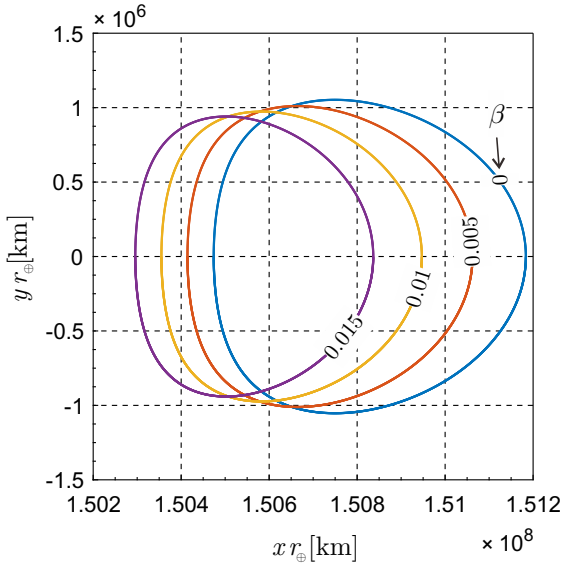

(a) $(\hat{\boldsymbol{x}} - \hat{\boldsymbol{y}})$ projection

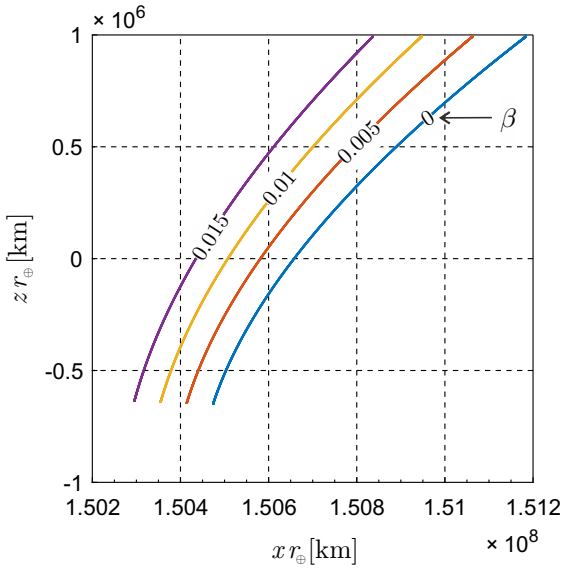

(b) $(\hat{\boldsymbol{x}} - \hat{\boldsymbol{z}})$ projection

Figure 4: Families of halo orbits around L_2-type AEPs with $u = 0.4$ and $\beta = \{0,\ 0.005,\ 0.01,\ 0.015\}$.

The non-integrability nature of Eqs. (15)–(17) prevents the artificial halo orbit from any analytical (exact) representation. However, as will be shown later, the solar sail formation control system requires an explicit description of the nominal trajectory. To this end, paralleling the procedure described in Ref. [63], a Fourier series-based solution with a least-square technique is now proposed to estimate the nominal trajectory with a reduced computational effort. The nominal trajectory is represented with an approximate trigonometric polynomial as

$$\boldsymbol{r}_h = \sum_{k=0}^{n} \left[\boldsymbol{c}_k \cos\left(k\,\omega_h\,t\right) + \boldsymbol{s}_k \sin\left(k\,\omega_h\,t\right)\right] \tag{18}$$

where ω_h is the angular frequency of the nominal halo orbit, and $\boldsymbol{r}_h$ is the (dimensionless) position vector of a generic point h at time t, with $[\boldsymbol{r}_h]_{\mathcal{T}} \triangleq [x_h,\, y_h,\, z_h]^{\mathrm{T}}$; see Fig. 5. In Eq. (18), $\boldsymbol{\ell} \triangleq \{\boldsymbol{c}_k, \boldsymbol{s}_k\}$ is the set of

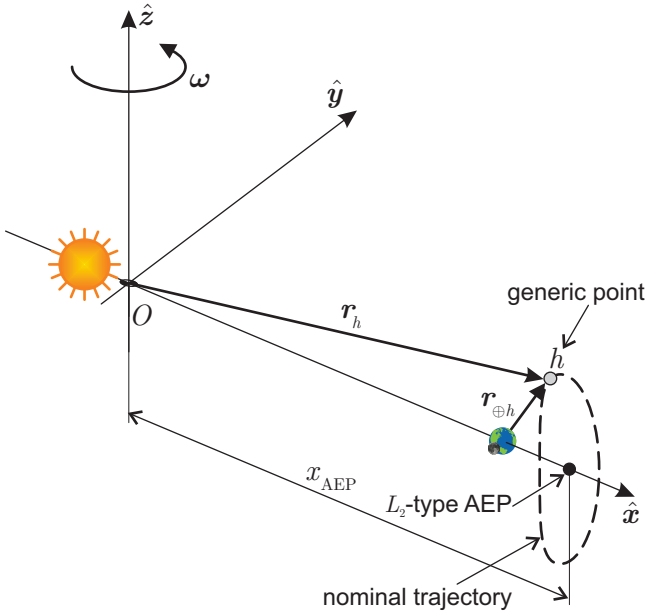

Figure 5: L_2-type AEP and nominal trajectory.

coefficients to be evaluated. For a given order n of the truncated series (18), the value of $\boldsymbol{\ell}$ may be found using an unconstrained least-square procedure, with the minimization index defined as

$$\boldsymbol{\ell} = \arg\,\min \left\{ \int_0^{T_h} \|\boldsymbol{X} - \boldsymbol{X}_h\|^2 \,\mathrm{d}t \right\} \tag{19}$$

where $\boldsymbol{X} \triangleq [\boldsymbol{r}^{\mathrm{T}},\, \dot{\boldsymbol{r}}^{\mathrm{T}}]^{\mathrm{T}}$ is the state vector along the trajectory, and $T_h \triangleq 2\,\pi/\omega_h$ is the period of the nominal halo orbit.

4. Solar sail formation design

Having analyzed the generation (and analytical approximation) of the nominal trajectory, we are now in a position to study the relative motion of a solar sail-based spacecraft formation. Let $\boldsymbol{\rho}_i \triangleq \boldsymbol{r}_i - \boldsymbol{r}_h$ denote the relative dimensionless position vector of the ith solar sail s_i with respect to the corresponding point h on the nominal trajectory. In particular, the nominal trajectory is obtained with an assigned value of both the sail lightness number $\beta = \beta_h$, and the reflectivity modulation ratio $u = u_h$. Note that the approximation of the vector $\boldsymbol{r}_h$ is given by Eq. (18). Moreover, let $\boldsymbol{r}_{\odot h}$ and $\boldsymbol{r}_{\oplus h}$ denote the position vectors from the Sun and the Earth to the generic point h on the nominal trajectory, respectively; see Fig. 6.

The dimensionless relative equation of motion of the spacecraft s_i, in the rotating reference frame $\mathcal{T}$, can be written as

$$\ddot{\boldsymbol{\rho}}_i + 2\,\boldsymbol{\omega} \times \dot{\boldsymbol{\rho}}_i = \frac{\partial\,\Omega_i}{\partial\,\boldsymbol{r}_i} - \frac{\partial\,\Omega_h}{\partial\,\boldsymbol{r}_h} + \boldsymbol{a}_i - \boldsymbol{a}_h \tag{20}$$

where $\boldsymbol{a}_h$ is the propulsive acceleration vector required by the sail at point h to follow the nominal trajectory with a Sun-facing attitude, that is

$$\boldsymbol{a}_h = \frac{\beta_h\,(1-\mu)\,(1-u_h/2)}{r_{\odot h}^2}\,\hat{\boldsymbol{r}}_{\odot h} \tag{21}$$

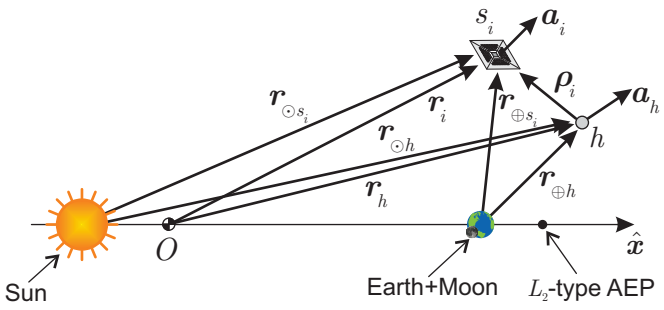

Figure 6: Schematization of the relative position vector between sail s_i and the nominal trajectory.

Because the solar sails operate in the neighbourhood of the nominal trajectory, the relative distance $\rho_i \triangleq \|\boldsymbol{\rho}_i\|$ is much smaller than $r_{\odot h} \triangleq \|\boldsymbol{r}_{\odot h}\|$. Moreover, the magnitude of the relative unit normal vector $\Delta\,\hat{\boldsymbol{n}}_i \triangleq \hat{\boldsymbol{n}}_i - \hat{\boldsymbol{n}}_h$, and the relative reflectivity ratio $\Delta\,u_i \triangleq u_i - u_h$ are both negligible at first-order. Accordingly, the relevant terms in Eq. (20) can be linearized around those of the nominal trajectory as

$$\boldsymbol{a}_i \simeq \boldsymbol{a}_h + \frac{\partial\,\boldsymbol{a}_h}{\partial\,\boldsymbol{r}_{\odot h}}\,\boldsymbol{\rho}_i + \frac{\partial\,\boldsymbol{a}_h}{\partial\,\hat{\boldsymbol{n}}_h}\,\Delta\,\hat{\boldsymbol{n}}_i + \frac{\partial\,\boldsymbol{a}_h}{\partial\,u_h}\,\Delta\,u_i \tag{22}$$

$$\frac{\partial\,\Omega_i}{\partial\,\boldsymbol{r}_i} \simeq \frac{\partial\,\Omega_h}{\partial\,\boldsymbol{r}_h} + \frac{\partial^2\,\Omega_h}{\partial\,\boldsymbol{r}_h^2}\,\boldsymbol{\rho}_i \tag{23}$$

where

$$\frac{\partial\,\boldsymbol{a}_h}{\partial\,\boldsymbol{r}_{\odot h}} = \frac{\beta_h\,(1-\mu)}{r_{\odot h}^3}\left\{\frac{u_h}{2}\,\left[(\hat{\boldsymbol{r}}_{\odot h}\,\hat{\boldsymbol{n}}_h^{\mathrm{T}}) + (\hat{\boldsymbol{n}}_h\cdot\hat{\boldsymbol{r}}_{\odot h})\,\mathbb{I}_3 - (\hat{\boldsymbol{n}}_h\cdot\hat{\boldsymbol{r}}_{\odot h})\,\left(\hat{\boldsymbol{r}}_{\odot h}\,\hat{\boldsymbol{r}}_{\odot h}^{\mathrm{T}}\right)\right]\right.$$

$$\left. + 2\,(1-u_h)\,\left[(\hat{\boldsymbol{n}}_h\cdot\hat{\boldsymbol{r}}_{\odot h})\,(\hat{\boldsymbol{n}}_h\,\hat{\boldsymbol{n}}_h^{\mathrm{T}}) - 2\,(\hat{\boldsymbol{n}}_h\cdot\hat{\boldsymbol{r}}_{\odot h})^2\,\left(\hat{\boldsymbol{n}}_h\,\hat{\boldsymbol{r}}_{\odot h}^{\mathrm{T}}\right)\right]\right\} \tag{24}$$

$$\frac{\partial\,\boldsymbol{a}_h}{\partial\,\hat{\boldsymbol{n}}_h} = \frac{\beta_h\,(1-\mu)}{r_{\odot h}^2}\left\{\frac{u_h}{2}\,\left(\hat{\boldsymbol{r}}_{\odot h}\,\hat{\boldsymbol{r}}_{\odot h}^{\mathrm{T}}\right) + (1-u_h)\left[2\,(\hat{\boldsymbol{n}}_h\cdot\hat{\boldsymbol{r}}_{\odot h})\,\left(\hat{\boldsymbol{n}}_h\,\hat{\boldsymbol{r}}_{\odot h}^{\mathrm{T}}\right) + (\hat{\boldsymbol{n}}_h\cdot\hat{\boldsymbol{r}}_{\odot h})^2\,\mathbb{I}_3\right]\right\} \tag{25}$$

$$\frac{\partial\,\boldsymbol{a}_h}{\partial\,u_h} = \frac{\beta_h\,(1-\mu)}{r_{\odot h}^2}\left[\frac{1}{2}\,(\hat{\boldsymbol{n}}_h\cdot\hat{\boldsymbol{r}}_{\odot h})\,\hat{\boldsymbol{r}}_{\odot h} - (\hat{\boldsymbol{n}}_h\cdot\hat{\boldsymbol{r}}_{\odot h})^2\,\hat{\boldsymbol{n}}_h\right] \tag{26}$$

$$\frac{\partial^2\,\Omega_h}{\partial\,\boldsymbol{r}_h^2} = \frac{(1-\mu)}{r_{\odot h}^3}\,\left(3\,\hat{\boldsymbol{r}}_{\odot h}\,\hat{\boldsymbol{r}}_{\odot h}^{\mathrm{T}} - \mathbb{I}_3\right) + \frac{\mu}{r_{\oplus h}^3}\,\left(3\,\hat{\boldsymbol{r}}_{\oplus h}\,\hat{\boldsymbol{r}}_{\oplus h}^{\mathrm{T}} - \mathbb{I}_3\right) + \mathrm{diag}\,(1,\,1,\,0) \tag{27}$$

The nominal trajectory around the L_2-type AEP is designed assuming the solar sail normal vector to lie along the Sun-sail line, hence

$$[\hat{\boldsymbol{n}}_h]_{\mathcal{T}} \equiv [\hat{\boldsymbol{r}}_{\odot h}]_{\mathcal{T}} = [x_h + \mu,\; y_h,\; z_h]^{\mathrm{T}} \tag{28}$$

$$[\hat{\boldsymbol{r}}_{\oplus h}]_{\mathcal{T}} = [x_h + \mu - 1,\; y_h,\; z_h]^{\mathrm{T}} \tag{29}$$

Recalling Eq. (2), the attitude angles necessary for the nominal trajectory are written as

$$\theta_h = \arcsin\,(\hat{\boldsymbol{n}}_h\cdot\hat{\boldsymbol{z}})\,, \qquad \phi_h = \arcsin\,[(\hat{\boldsymbol{n}}_h\times\hat{\boldsymbol{z}})\,/\,\|\hat{\boldsymbol{n}}_h\times\hat{\boldsymbol{z}}\|\cdot\hat{\boldsymbol{x}}] \tag{30}$$

where $\hat{\boldsymbol{n}}_h$ is given by Eq. (28). Accordingly, the relative normal vector $\Delta\,\hat{\boldsymbol{n}}_i$ in Eq. (22) can be further linearized as

$$\Delta\,\hat{\boldsymbol{n}}_i \simeq \frac{\partial\,\hat{\boldsymbol{n}}_h}{\partial\,[\theta_h,\,\phi_h]}\,[\Delta\,\theta_i,\,\Delta\,\phi_i]^{\mathrm{T}} \tag{31}$$

where $\Delta\,\theta_i \triangleq \theta_i - \theta_h$ and $\Delta\,\phi_i \triangleq \phi_i - \phi_h$ are the relative sail attitude angles, while the Jacobian matrix is

$$\frac{\partial\,\hat{\boldsymbol{n}}_h}{\partial\,[\theta_h,\,\phi_h]} = \begin{bmatrix} -\sin\,\theta_h\,\cos\,\phi_h & -\cos\,\theta_h\,\sin\,\phi_h \\ -\sin\,\theta_h\,\sin\,\phi_h & \cos\,\theta_h\,\cos\,\phi_h \\ \cos\,\theta_h & 0 \end{bmatrix} \tag{32}$$

Substituting Eqs. (22)–(32) into Eq. (20), the (dimensionless) linear differential equation of the relative motion of the ith sail s_i, with respect to the generic point h on the nominal trajectory, can be written in a compact form as

$$\ddot{\boldsymbol{\rho}}_i + 2\,\mathbb{M}_v\,\dot{\boldsymbol{\rho}}_i + \mathbb{M}_p\,\boldsymbol{\rho}_i = \mathbb{M}_h\,\boldsymbol{u}_i \tag{33}$$

where

$$\mathbb{M}_v \triangleq \begin{bmatrix} 0 & -1 & 0 \\ 1 & 0 & 0 \\ 0 & 0 & 0 \end{bmatrix} \tag{34}$$

$$\mathbb{M}_p \triangleq -\frac{\partial^2\,\Omega_h}{\partial\,\boldsymbol{r}_h^2} - \frac{\partial\,\boldsymbol{a}_h}{\partial\,\boldsymbol{r}_{\odot h}} \tag{35}$$

$$\mathbb{M}_h \triangleq \left[\frac{\partial\,\boldsymbol{a}_h}{\partial\,\hat{\boldsymbol{n}}_h}\,\frac{\partial\,\hat{\boldsymbol{n}}_h}{\partial\,[\theta_h,\phi_h]},\,\frac{\partial\,\boldsymbol{a}_h}{\partial\,u_h}\right] \tag{36}$$

while $\boldsymbol{u}_i$ is the control input of the generic solar sail s_i, defined as

$$\boldsymbol{u}_i \triangleq [\Delta\,\theta_i,\,\Delta\,\phi_i,\,\Delta\,u_i]^{\mathrm{T}} \tag{37}$$

In the analysis to follow, cooperative strategies for the formation system described by Eq. (33) will be designed such that all of the solar sails in formation reach consensus as $t \to +\infty$.

5. Cooperative formation control

Distributed coordinated control algorithms are now considered for a formation structure with $N \geq 3$ solar sail-based spacecraft, relying on local neighbor-to-neighbor interactions. In case of data transmission through local sensing [64, 65], the solar sails in a formation are likely to be equipped by sensors with a limited field of view only, which induce unidirectional communication topologies. To model such a behavior, the information exchange among the spacecraft in the formation is assumed to be characterized by a generic directed graph [66].

According to the procedure discussed in Ref. [63], a few pertinent concepts of algebraic graph theory [66] are first briefly summarized for the sake of completeness. A directed graph $\mathcal{G}$ consists of a finite non-empty vertex set $\mathcal{V} \triangleq \{\upsilon_1, \ldots, \upsilon_N\}$, an edge set $\mathcal{E} \triangleq \{(\upsilon_1, \upsilon_2), \ldots, (\upsilon_{N-1}, \upsilon_N)\} \subseteq \mathcal{V} \times \mathcal{V}$, and a weighted adjacency matrix $\mathbb{W} = [w_{ij}] \in \mathbb{R}^{N\times N}$. An edge $(\upsilon_i, \upsilon_j) \in \mathcal{E}$ in a directed graph implies that the information flows from vertex υ_i to υ_j, but not necessarily vice versa. When there is an edge from vertex υ_i to vertex υ_j, then υ_i is defined as the parent vertex, while υ_j is defined as the child vertex. The generic entry of a weighted adjacency matrix $\mathbb{W}$ is $w_{ij} > 0$, $\forall\,(\upsilon_j, \upsilon_i) \in \mathcal{E}$ with $i \neq j$, and $w_{ii} = 0$. The Laplacian matrix $\mathbb{L} = [l_{ij}] \in \mathbb{R}^{N\times N}$ associated with $\mathbb{W}$ is defined such that $l_{ij} = -w_{ij}$ and $l_{ii} = \sum_{j=1}^{N} w_{ij}, \forall\, i \neq j$. A rooted directed spanning tree is constituted by edges that connect all the vertices; see Fig. 7. Note that a directed graph has a rooted spanning tree if and only if there exists at least one vertex having a directed path to all of the other vertices. Finally, the topology is assumed to be fixed throughout the paper and the Laplacian matrix $\mathbb{L}$ is constant.

In modeling the topology of the solar sail relative motion, each sail is represented by a vertex, while the interactions between two generic sails are characterized by a weighted directed edge. In the next sections, distributed control strategies will be developed in both the leaderless case and the virtual-leader case respectively, such that the overall consensus will be reached.

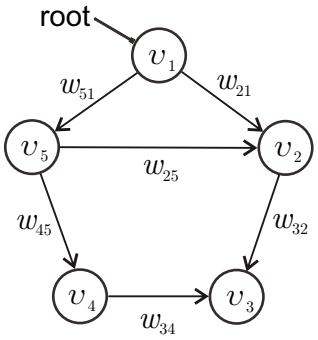

Figure 7: Schematization of a directed topology graph including a rooted spanning tree.

5.1. Leaderless case

Consider first the case in which a centralized leadership is absent and the solar sail-based spacecraft in formation are required to maintain a desired relative configuration. Such a sort of leaderless formation structure is said to follow a behavior approach [67], which is typical in cluster flight or swarm missions [68, 69, 70], where the control law is designed for each vehicle such that the solar sails have a common formation center c. In this case, more flexibility, reliability, and robustness can be guaranteed than those in a centralized leader-follower configuration [41].

Let $\{\boldsymbol{\rho}_{ci}, \dot{\boldsymbol{\rho}}_{ci}\} \in \mathbb{R}^3 \times \mathbb{R}^3$, with $i = 1, \ldots, N$, be the desired relative state of the solar sail s_i with respect to the formation center c; see Fig. 8. If subscript $j \neq i$ denotes the sail s_j, a consensus (the control objective) is said to be reached when

$$(\boldsymbol{\rho}_i - \boldsymbol{\rho}_{ci}) \to (\boldsymbol{\rho}_j - \boldsymbol{\rho}_{cj}) \to \boldsymbol{\rho}_c \quad \cap \quad (\dot{\boldsymbol{\rho}}_i - \dot{\boldsymbol{\rho}}_{ci}) \to (\dot{\boldsymbol{\rho}}_j - \dot{\boldsymbol{\rho}}_{cj}) \to \mathbf{0}_3 \tag{38}$$

where $\boldsymbol{\rho}_c$ is the relative position vector of the formation center with respect to the point h on the nominal (artificial halo orbit) trajectory; see Fig. 8. In this case, the formation center is assumed to be initially unspecified. Indeed, it is determined by all of the solar sails through a negotiation process.

For convenience, introduce the auxiliary vectors $\boldsymbol{q}_i \triangleq \boldsymbol{\rho}_i - \boldsymbol{\rho}_{ci}$ and $\dot{\boldsymbol{q}}_i \triangleq \dot{\boldsymbol{\rho}}_i - \dot{\boldsymbol{\rho}}_{ci}$, so that Eq. (38) can be rewritten as

$$\boldsymbol{q}_i \to \boldsymbol{q}_j \to \boldsymbol{\rho}_c \quad \cap \quad \dot{\boldsymbol{q}}_i \to \dot{\boldsymbol{q}}_j \to \mathbf{0}_3 \tag{39}$$

and assume a cooperative control law in Eq. (33), defined as

$$\boldsymbol{u}_i = \mathbb{M}_h^{-1} \left\{ \ddot{\boldsymbol{\rho}}_{ci} + 2\,\mathbb{M}_v\,\dot{\boldsymbol{\rho}}_i + \mathbb{M}_p\,\boldsymbol{\rho}_i - \alpha\,\dot{\boldsymbol{q}}_i - \sum_{j=1}^{N} w_{ij}\,\left[\left(\boldsymbol{q}_i - \boldsymbol{q}_j\right) + \gamma\left(\dot{\boldsymbol{q}}_i - \dot{\boldsymbol{q}}_j\right) \right] \right\} \tag{40}$$

where $\{\alpha,\, \gamma\} \in \mathbb{R}^+$, and the matrices $\mathbb{M}_p$, $\mathbb{M}_v$, and $\mathbb{M}_h$ are given by Eqs. (34)–(36).

Theorem 1: Using the control law (40) with the solar sail formation structure represented by Eq. (33), consensus (that is, conditions (39)) is asymptotically achieved if the topology graph $\mathcal{G}$ includes (at least) a spanning tree, and the coefficient γ satisfies

$$\gamma > \max_{\{i \,|\, \mathrm{Re}\,(\lambda_i) < 0\}} \sqrt{\frac{2}{|\lambda_i|\,\cos\left[\dfrac{\pi}{2} - \arctan\,\dfrac{-\,\mathrm{Re}\,(\lambda_i)}{\mathrm{Im}\,(\lambda_i)}\right]}} \tag{41}$$

where λ_i is the ith eigenvalue of matrix $-\mathbb{L}$.

Proof: With the control input of Eq. (40), the second-order differential equation for $\boldsymbol{q}_i$ can be written as

$$\ddot{\boldsymbol{q}}_i + \alpha\,\dot{\boldsymbol{q}}_i + \sum_{j=1}^{N} w_{ij}\,\left[\left(\boldsymbol{q}_i - \boldsymbol{q}_j\right) + \gamma\,\left(\dot{\boldsymbol{q}}_i - \dot{\boldsymbol{q}}_j\right) \right] = \mathbf{0}_3 \tag{42}$$

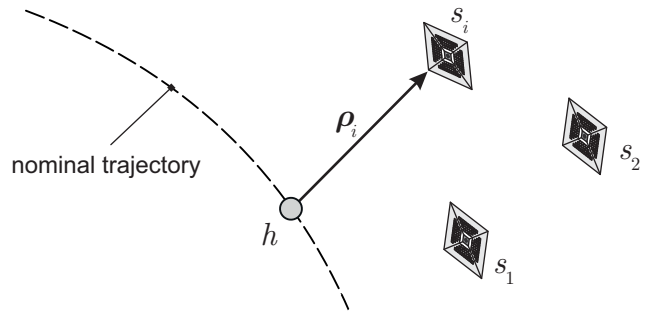

(a) Initial relative motion at $t = t_0$

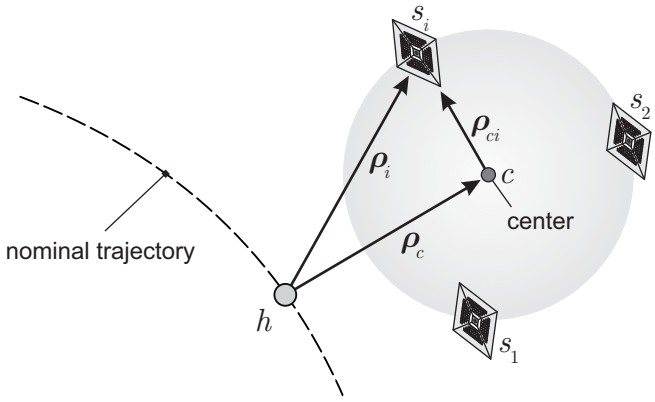

(b) Final (desired) relative motion as $t \to +\infty$

Figure 8: Schematic illustration of the leaderless solar sail formation structure.

which can be collected into a compact state-space form by introducing the auxiliary vector $\boldsymbol{q} \triangleq [\boldsymbol{q}_1^{\mathrm{T}}, \ldots, \boldsymbol{q}_N^{\mathrm{T}}]^{\mathrm{T}}$, i.e.

$$[\dot{\boldsymbol{q}}^{\mathrm{T}},\, \ddot{\boldsymbol{q}}^{\mathrm{T}}]^{\mathrm{T}} = (\mathbb{Q} \otimes \mathbb{I}_3)\; [\boldsymbol{q}^{\mathrm{T}},\, \dot{\boldsymbol{q}}^{\mathrm{T}}]^{\mathrm{T}} \tag{43}$$

where $\otimes$ denotes the Kronecker product, and the matrix $\mathbb{Q} \in \mathbb{R}^{2\,N \times 2\,N}$ is defined as

$$\mathbb{Q} \triangleq \begin{bmatrix} \mathbb{O}_N & \mathbb{I}_N \\ -\mathbb{L} & -\alpha\, \mathbb{I}_N - \gamma\, \mathbb{L} \end{bmatrix} \tag{44}$$

The eigenvalues of $\mathbb{Q}$ are found by enforcing the condition $\det\,(\eta\, \mathbb{I}_{2\,N} - \mathbb{Q}) = 0$, which leads to

$$\det\, \left[\left(\eta^2 + \alpha\, \eta \right)\, \mathbb{I}_N + (1 + \gamma\, \eta)\, \mathbb{L} \right] = 0 \tag{45}$$

The roots of Eq. (45) are calculated by solving $\eta^2 + \alpha\, \eta = \lambda_i\, (1 + \gamma\, \eta)$, and the eigenvalues of $\mathbb{Q}$ are given by

$$\eta_{i\,\pm} = \frac{\gamma\, \lambda_i - \alpha \pm \sqrt{(\gamma\, \lambda_i - \alpha)^2 + 4\, \lambda_i}}{2} \tag{46}$$

If there exists a spanning tree in the communication topology, then $-\mathbb{L}$ has a simple zero eigenvalue, while all other eigenvalues have negative real parts [65]. In this case, it can be drawn from Eq. (46) that all of the eigenvalues of $\mathbb{Q}$ have negative real parts, i.e. $\mathrm{Re}\,(\eta_i) < 0$, and the system is asymptotically stable if the inequality in Eq. (41) holds true.

Having discussed the conditions under which a consensus may be reached, another important problem is to find the equilibrium state for the solar sails. To that end, consider the linear system represented by Eq. (43), whose state-transition matrix is

$$\mathrm{e}^{(\mathbb{Q} \otimes \mathbb{I}_3)\, t} = \mathrm{e}^{(\mathbb{Q}\, t) \otimes \mathbb{I}_3} = \mathrm{e}^{\mathbb{Q}\, t} \otimes \mathbb{I}_3 \tag{47}$$

As is shown in Ref. [65], as $t \to +\infty$ the following relationship holds

$$\lim_{t\to+\infty} \mathrm{e}^{\mathbb{Q}\,t} = \begin{bmatrix} \mathbf{1}_N\,\boldsymbol{p}^{\mathrm{T}} & \frac{1}{\alpha}\mathbf{1}_N\,\boldsymbol{p}^{\mathrm{T}} \\ \mathbb{O}_N & \mathbb{O}_N \end{bmatrix} \tag{48}$$

where $\mathbf{1}_N \in \mathbb{R}^N$ denotes the column vector of all ones, and $\boldsymbol{p} \in \mathbb{R}^N$ is a left eigenvector of the matrix $-\mathbb{L}$ associated with eigenvalue 0, such that $\boldsymbol{p}\cdot\mathbf{1}_N = 1$. According to Eqs. (43), (47) and (48), it follows that

$$\boldsymbol{q} \to [(\mathbf{1}_N\,\boldsymbol{p}^{\mathrm{T}}) \otimes \mathbb{I}_3]\;\boldsymbol{q}_c + \frac{1}{\alpha}\,[(\mathbf{1}_N\,\boldsymbol{p}^{\mathrm{T}}) \otimes \mathbb{I}_3]\;\dot{\boldsymbol{q}}_c, \qquad \dot{\boldsymbol{q}} \to \mathbf{0}_{3\,N} \tag{49}$$

where $\boldsymbol{q}_c \triangleq [\boldsymbol{q}_{c1}^{\mathrm{T}}, \ldots, \boldsymbol{q}_{cN}^{\mathrm{T}}]^{\mathrm{T}}$ is the initial value of $\boldsymbol{q}$.

Let p_i be the ith component of the left eigenvector $\boldsymbol{p}$, it can be verified from Eq. (49) that the final position vector $\boldsymbol{\rho}_c$ of the formation center c relative to the generic point h on the nominal trajectory is

$$\boldsymbol{\rho}_c = \lim_{t\to+\infty} \boldsymbol{q} = \sum_{i=1}^{N} p_i \left(\boldsymbol{q}_{ci} + \frac{1}{\alpha}\,\dot{\boldsymbol{q}}_{ci}\right) \tag{50}$$

which amounts to stating that consensus is guaranteed in the sense of the conditions given by Eq. (39). □

Note that with the control law given by Eq. (40), the final location of the formation center is defined by a weighted average of the initial states of all solar sails. **Theorem 1** also indicates that $(\boldsymbol{\rho}_i - \boldsymbol{\rho}_j) \to (\boldsymbol{\rho}_{ci} - \boldsymbol{\rho}_{cj})$. Therefore, $\boldsymbol{\rho}_{ci}$ and $\boldsymbol{\rho}_{cj}$ can be selected so as to acquire a desired separation between the solar sails s_i and s_j.

5.2. Virtual-leader case

In some scientific missions, such as those involving synthesizing interferometers [39, 70], it is necessary to prescribe the state relative to some reference point for each vehicle, and treat the entire formation as a single entity [42, 71]. In those cases, a reference point plays the role of virtual leader (v) of the solar sail formation structure, around which a desired relative configuration can be formed by properly designing the cooperative control strategy. To that end, a distributed control algorithm gives good performance especially when the state of the virtual leader cannot be known precisely due to the limitations on the communication bandwidth and the sensing range. Such a control system will now be designed in two different subcases, depending on whether i) all of the sails or ii) only a subgroup of the sails can share information of the virtual leader state.

Let $\boldsymbol{\rho}_v$ denote the position vector of the virtual leader v relative to the generic point h on the nominal trajectory, and $\{\boldsymbol{\rho}_{vi}, \dot{\boldsymbol{\rho}}_{vi}\} \in \mathbb{R}^3 \times \mathbb{R}^3$ be the desired relative state of the ith solar sail s_i with respect to the virtual leader; see Fig. 9. In contrast to the leaderless case, the position vector $\boldsymbol{\rho}_v$ is here specified in advance and is possibly time-varying. The goal of the cooperative control law is to drive each solar sail in formation toward the desired relative trajectory, while guaranteeing a group synchronization during the maneuver, viz.

$$\boldsymbol{\rho}_i - \boldsymbol{\rho}_{vi} \to \boldsymbol{\rho}_j - \boldsymbol{\rho}_{vj} \to \boldsymbol{\rho}_v \quad \cap \quad \dot{\boldsymbol{\rho}}_i - \dot{\boldsymbol{\rho}}_{vi} \to \dot{\boldsymbol{\rho}}_j - \dot{\boldsymbol{\rho}}_{vj} \to \boldsymbol{\rho}_v \tag{51}$$

5.2.1. Full access to the virtual leader state

When the information of the virtual leader state is available to all of the solar sails, the consensus protocol is designed as

$$\boldsymbol{u}_i = \mathbb{M}_h^{-1} \left\{ \ddot{\boldsymbol{\rho}}_v + \ddot{\boldsymbol{\rho}}_{vi} + 2\,\mathbb{M}_v\,\dot{\boldsymbol{\rho}}_i + \mathbb{M}_p\,\boldsymbol{\rho}_i - \sigma\;(\boldsymbol{e}_i + \zeta\,\dot{\boldsymbol{e}}_i) - \sum_{j=1}^{N} w_{ij}\;[(\boldsymbol{e}_i - \boldsymbol{e}_j) + \zeta\;(\dot{\boldsymbol{e}}_i - \dot{\boldsymbol{e}}_j)] \right\} \tag{52}$$

where the parameters $\{\sigma, \zeta\} \in \mathbb{R}^+$, while the position error and the velocity error of the sail s_i are $\boldsymbol{e}_i \triangleq \boldsymbol{\rho}_i - \boldsymbol{\rho}_v - \boldsymbol{\rho}_{vi}$ and $\dot{\boldsymbol{e}}_i \triangleq \dot{\boldsymbol{\rho}}_i - \dot{\boldsymbol{\rho}}_v - \dot{\boldsymbol{\rho}}_{vi}$, respectively.

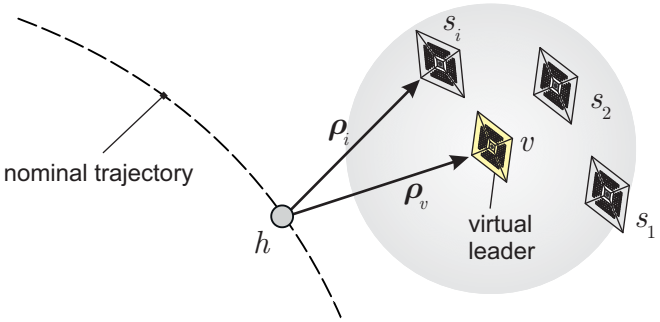

(a) Initial relative motion at $t = t_0$

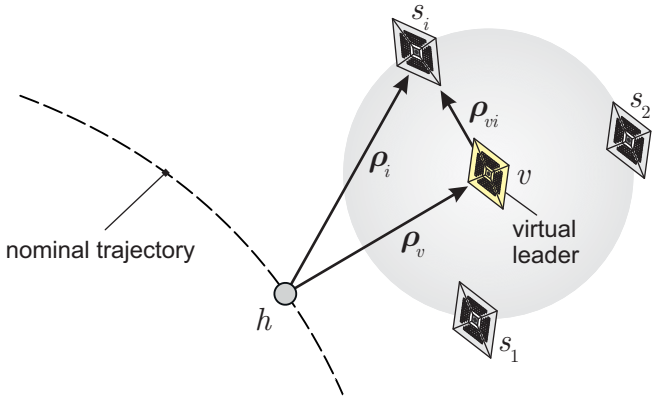

(b) Final (desired) relative motion as $t \to +\infty$

Figure 9: Schematic illustration of the virtual-leader solar sail formation flying.

Theorem 2: Using the control law given by Eq. (52) for the solar sail-based formation structure described by Eq. (33), consensus (that is, $\boldsymbol{e}_i \to \boldsymbol{e}_j \to \mathbf{0}_3$ and $\dot{\boldsymbol{e}}_i \to \dot{\boldsymbol{e}}_j \to \mathbf{0}_3$) is asymptotically achieved if the topology graph $\mathcal{G}$ includes (at least) a spanning tree and the coefficient ζ satisfies

$$\zeta > \max_{i=1,\ldots,N} \sqrt{\frac{2}{|\nu_i| \cos\left[\frac{\pi}{2} - \arctan\frac{-\mathrm{Re}\,(\nu_i)}{\mathrm{Im}\,(\nu_i)}\right]}} \tag{53}$$

where $\nu_i = -\sigma + \lambda_i$ is the ith eigenvalue of $-(\sigma\,\mathbb{I}_N + \mathbb{L})$.

Proof: Using the control law (52) and bearing in mind the relative motion dynamics given by Eq. (33), the differential equation for the position error $\boldsymbol{e}_i$ can be written as

$$\ddot{\boldsymbol{e}}_i + \sigma\,(\boldsymbol{e}_i + \zeta\,\dot{\boldsymbol{e}}_i) + \sum_{j=1}^{N} w_{ij}\,[(\boldsymbol{e}_i - \boldsymbol{e}_j) + \zeta\,(\dot{\boldsymbol{e}}_i - \dot{\boldsymbol{e}}_j)] = \mathbf{0} \tag{54}$$

By introducing the auxiliary vector $\boldsymbol{e} \triangleq [\boldsymbol{e}_1^{\mathrm{T}}, \ldots, \boldsymbol{e}_N^{\mathrm{T}}]^{\mathrm{T}}$, a compact form of Eq. (54) is given by

$$[\dot{\boldsymbol{e}}^{\mathrm{T}},\, \ddot{\boldsymbol{e}}^{\mathrm{T}}]^{\mathrm{T}} = (\mathbb{E} \otimes \mathbb{I}_3)\,[\boldsymbol{e}^{\mathrm{T}},\, \dot{\boldsymbol{e}}^{\mathrm{T}}]^{\mathrm{T}} \tag{55}$$

where the matrix $\mathbb{E} \in \mathbb{R}^{2\,N \times 2\,N}$ is defined as

$$\mathbb{E} \triangleq \begin{bmatrix} \mathbb{O}_N & \mathbb{I}_N \\ -(\sigma\,\mathbb{I}_N + \mathbb{L}) & -\zeta\,(\sigma\,\mathbb{I}_N + \mathbb{L}) \end{bmatrix} \tag{56}$$

The eigenvalues of $\mathbb{E}$ are

$$\xi_{i\pm} = \frac{\zeta\,\nu_i \pm \sqrt{\zeta^2\,\nu_i^2 + 4\,\nu_i}}{2} \tag{57}$$

Paralleling the approach in the leaderless case, it is straightforward to see that each eigenvalue ξ_i (with $i = 1, \ldots, N$) has a negative real part if Eq. (53) is satisfied, which implies $\boldsymbol{e}_i \to \mathbf{0}_3$ and $\dot{\boldsymbol{e}}_i \to \mathbf{0}_3$. In particular, a synchronized transition, i.e. $\boldsymbol{e}_i \to \boldsymbol{e}_j \to \mathbf{0}_3$ and $\dot{\boldsymbol{e}}_i \to \dot{\boldsymbol{e}}_j \to \mathbf{0}_3$, can be guaranteed when the information exchange topology has a spanning tree due to the state feedback couplings among the sails [65]. □

5.2.2. Partial access to the virtual leader state

The cooperative control algorithm given by Eq. (52) assumes the virtual leader state to be available to each solar sail, which is usually unrealistic in practice. Considering the fact that the solar sail-based spacecraft usually conveys a rather limited payload and communication instrument mass, it is possible that the information of the virtual leader state can only be measured by the onboard sensors of a part of the sails in formation, and these sails may not have a directed path to all the others.

Such a circumstance necessitates an alternative algorithm accounting for the general case where only a part of formation have access to the virtual leader state. To this end, the consensus strategy is proposed in the form

$$\begin{aligned}\boldsymbol{u}_i = \mathbb{M}_h^{-1}\Bigg\{ & \ddot{\boldsymbol{\rho}}_{vi} + 2\,\mathbb{M}_v\,\dot{\boldsymbol{\rho}}_i + \mathbb{M}_p\,\boldsymbol{\rho}_i + \frac{1}{\sum\limits_{j=0}^{N} w_{ij}} \sum_{j=1}^{N} w_{ij}\,\left[\left(\ddot{\boldsymbol{\rho}}_j - \ddot{\boldsymbol{\rho}}_{vj}\right) - \delta\,\left(\boldsymbol{e}_i - \boldsymbol{e}_j\right) - \kappa\,\left(\dot{\boldsymbol{e}}_i - \dot{\boldsymbol{e}}_j\right)\right] \\ & + \frac{1}{\sum\limits_{j=0}^{N} w_{ij}}\,w_{vi}\,\left(\ddot{\boldsymbol{\rho}}_v - \delta\,\boldsymbol{e}_i - \kappa\,\dot{\boldsymbol{e}}_i\right)\Bigg\}\end{aligned} \tag{58}$$

where $\{\delta,\,\kappa\} \in \mathbb{R}^+$, $w_{i0} > 0$, $\forall\, i = 0, \ldots, N$, if the sail s_i has access to the state of the virtual leader and $w_{i0} = 0$ otherwise. Note that the virtual leader is treated as a virtual solar sail with index 0.

Theorem 3: Using the control law of Eq. (58) for the solar sail-based formation system described by Eq. (33), consensus (that is, $\boldsymbol{e}_i \to \boldsymbol{e}_j \to \mathbf{0}_3$ and $\dot{\boldsymbol{e}}_i \to \dot{\boldsymbol{e}}_j \to \mathbf{0}_3$) is asymptotically achieved if the virtual leader v is the root that has a path to each solar sail in formation.

Proof: With the control input of Eq. (58), it can be derived from Eq. (33) that

$$\begin{aligned}\sum_{j=0}^{N} w_{ij}\,\left(\ddot{\boldsymbol{\rho}}_i - \ddot{\boldsymbol{\rho}}_{vi}\right) &= \sum_{j=1}^{N} w_{ij}\,\left[\left(\ddot{\boldsymbol{\rho}}_j - \ddot{\boldsymbol{\rho}}_{vj}\right) - \delta\,\left(\boldsymbol{e}_i - \boldsymbol{e}_j\right) - \kappa\,\left(\dot{\boldsymbol{e}}_i - \dot{\boldsymbol{e}}_j\right)\right] + w_{i0}\,\left(\ddot{\boldsymbol{\rho}}_v - \delta\,\boldsymbol{e}_i - \kappa\,\dot{\boldsymbol{e}}_i\right) \\ &= \sum_{j=0}^{N} w_{ij}\,\left[\left(\ddot{\boldsymbol{\rho}}_j - \ddot{\boldsymbol{\rho}}_{vj}\right) - \delta\,\left(\boldsymbol{e}_i - \boldsymbol{e}_j\right) - \kappa\,\left(\dot{\boldsymbol{e}}_i - \dot{\boldsymbol{e}}_j\right)\right]\end{aligned} \tag{59}$$

Let $\boldsymbol{\epsilon}_i \triangleq \sum\limits_{j=0}^{N} w_{ij}\,\left(\boldsymbol{e}_i - \boldsymbol{e}_j\right)$, and recall the identity $\boldsymbol{\rho}_i - \boldsymbol{\rho}_{vi} - \boldsymbol{\rho}_j + \boldsymbol{\rho}_{vj} = \boldsymbol{e}_i - \boldsymbol{e}_j$. Then Eq. (59) becomes

$$\ddot{\boldsymbol{\epsilon}}_i + \delta\,\dot{\boldsymbol{\epsilon}}_i + \kappa\,\boldsymbol{\epsilon}_i = 0 \tag{60}$$

Since $\delta > 0$ and $\kappa > 0$, it follows from Eq. (60) that $\boldsymbol{\epsilon}_i \to \mathbf{0}_3$ and $\dot{\boldsymbol{\epsilon}}_i \to \mathbf{0}_3$ as $t \to +\infty$. For convenience, introduce the vector $\boldsymbol{l} \triangleq [l_{10}, \ldots, l_{N0}]^{\mathrm{T}} \in \mathbb{R}^N$, with $l_{i0} = -w_{i0}$, and let $\widetilde{\mathbb{L}} \triangleq [\mathbf{0}_N^{\mathrm{T}},\, 0;\, \mathbb{L},\, \boldsymbol{l}] \in \mathbb{R}^{(N+1)\times(N+1)}$ be the extended Laplacian matrix involving the virtual leader. It is straightforward to verify that $\left(\widetilde{\mathbb{L}} \otimes \mathbb{I}_3\right)\,\tilde{\boldsymbol{e}} \to \mathbf{0}_{3\,N}$ and $\left(\widetilde{\mathbb{L}} \otimes \mathbb{I}_3\right)\,\dot{\tilde{\boldsymbol{e}}} \to \mathbf{0}_{3\,N}$, where $\tilde{\boldsymbol{e}} \triangleq [\boldsymbol{e}_0^{\mathrm{T}},\, \boldsymbol{e}^{\mathrm{T}}]^{\mathrm{T}}$. Note that for the virtual leader, the state errors $\boldsymbol{e}_0 \equiv \mathbf{0}_3$ and $\dot{\boldsymbol{e}}_0 \equiv \mathbf{0}_3$. If the virtual leader has a path to each solar sail, then the information exchange topology involving the virtual leader includes a rooted spanning tree, which further results in $\boldsymbol{e}_i \to \boldsymbol{e}_j \to \boldsymbol{e}_0 = \mathbf{0}_3$ and $\dot{\boldsymbol{e}}_i \to \dot{\boldsymbol{e}}_j \to \boldsymbol{e}_0 = \mathbf{0}_3$. □

In contrast to the case in which the virtual leader state is accessible to all of the solar sails, Eq. (58) requires the acceleration of the neighbor sail, which may be calculated by numerical differentiation when onboard measurement is unavailable. For example, in the simplest case, $\ddot{\boldsymbol{\rho}}_j$ on the right side of Eq. (58) can be approximated by $\left(\dot{\boldsymbol{\rho}}_j\,[k+1]-\dot{\boldsymbol{\rho}}_j\,[k]\right)/\tau$, where k is the discrete-time index, and τ is the sampling interval. Other sampling algorithms can also be adopted such as the Runge-Kutta method.

6. Mission application

To illustrate the performance of the proposed cooperative control laws, a formation mission scenario consisting of three solar sails ($N=3$) around an artificial halo orbit centered at the Sun-[Earth+Moon] L_2-type AEP is now discussed. The nominal trajectory is obtained with $u_h=0.4$ and $\beta_h=0.01$. In this example, the solar sail relative trajectories with respect to the formation center track a projected circular orbit (PCO) with a radius $R\triangleq 10\,\text{km}$. Accordingly, for the leaderless case (see Fig. 8), the PCO parametric representation of the sail s_i (with $i\in\{1,2,3\}$) is assumed to have the following algebraic form

$$\boldsymbol{\rho}_{ci}=(R/r_\oplus)\,[0,\,\cos\,(\omega_h\,t+\varphi_i)\,,\,\sin\,(\omega_h\,t+\varphi_i)]^{\mathrm{T}} \tag{61}$$

whereas for the virtual-leader case (see Fig. 9) the PCO parametric representation is

$$\boldsymbol{\rho}_{vi}=(R/r_\oplus)\,[0,\,\cos\,(\omega_h\,t+\varphi_i)\,,\,\sin\,(\omega_h\,t+\varphi_i)]^{\mathrm{T}} \tag{62}$$

where $\varphi_i=(2/3)\,(i-1)\,\pi$ is the phase angle of the PCO.

In this case, the approximation of the nominal trajectory by a 6th-order Fourier series ($n=6$) is illustrated in Fig. 10, while the dimensionless coefficients $\{\boldsymbol{c}_k,\boldsymbol{s}_k\}$ of Eq. (18), evaluated in the least-square sense, are listed in Tab 1.

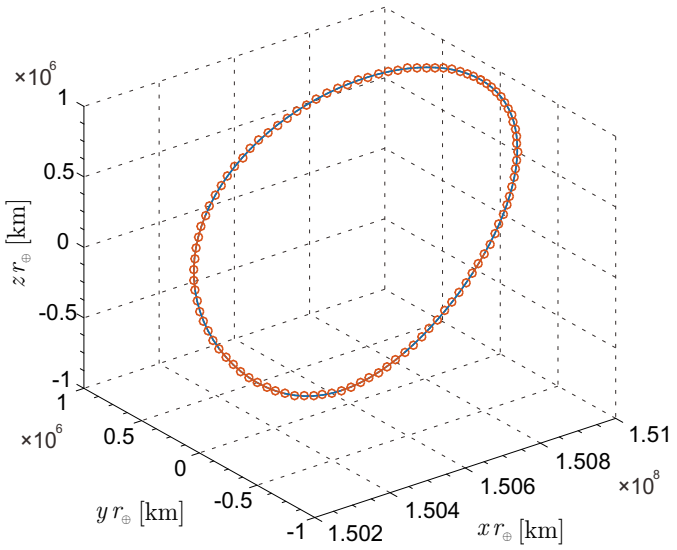

Figure 10: Nominal trajectory: approximate form (circles) vs. the numerical solution (solid line).

The accuracy of the 6th-order Fourier series approximation is confirmed by Fig. 11, which shows the time variation of the dimensionless (distance) error $\Delta\tilde{r}\triangleq(\|\boldsymbol{r}\|-\|\boldsymbol{r}_h\|)\,/\,\|\boldsymbol{r}\|$. According to Fig. 11, the maximum value of $|\Delta\tilde{r}|$ is less than 5×10^{-7}, indicating a good accuracy of the analytical approximation.

6.1. Leaderless case

Consider first the leaderless case in which a centralized leadership is absent and the formation center is not *a priori* specified. To evaluate the controller performance of Eq. (40), introduce the error indices $\boldsymbol{e}_{ij}\triangleq\boldsymbol{q}_i-\boldsymbol{q}_j$ and $\dot{\boldsymbol{e}}_{ij}\triangleq\dot{\boldsymbol{q}}_i-\dot{\boldsymbol{q}}_j$, with initial values reported in Tab. 2.

Table 1: Coefficients of the 6th-order Fourier series approximation of the nominal trajectory, see Eq. (18).

k	$\boldsymbol{c}_k$	$\boldsymbol{s}_k$
0	$\left[1.0070,\, 3.0854\times10^{-8},\, 1.7412\times10^{-3}\right]^{\mathrm{T}}$	$[0,\, 0,\, 0]^{\mathrm{T}}$
1	$\left[2.0039\times10^{-3},\, 3.3922\times10^{-7},\, 5.3430\times10^{-3}\right]^{\mathrm{T}}$	$\left[-2.2928\times10^{-9},\, -6.5287\times10^{-3},\, 1.2619\times10^{-7}\right]^{\mathrm{T}}$
2	$\left[6.5432\times10^{-5},\, -5.3794\times10^{-8},\, -5.3612\times10^{-4}\right]^{\mathrm{T}}$	$\left[1.9804\times10^{-9},\, 5.2543\times10^{-4},\, -3.2178\times10^{-8}\right]^{\mathrm{T}}$
3	$\left[-2.2999\times10^{-5},\, 3.5717\times10^{-8},\, 1.0509\times10^{-4}\right]^{\mathrm{T}}$	$\left[-1.8103\times10^{-9},\, -1.0514\times10^{-4},\, 1.4718\times10^{-8}\right]^{\mathrm{T}}$
4	$\left[6.8071\times10^{-6},\, -6.7082\times10^{-9},\, -2.4949\times10^{-5}\right]^{\mathrm{T}}$	$\left[-1.8024\times10^{-9},\, 2.5228\times10^{-5},\, -9.8589\times10^{-9}\right]^{\mathrm{T}}$
5	$\left[-2.0513\times10^{-6},\, 2.1746\times10^{-8},\, 6.5864\times10^{-6}\right]^{\mathrm{T}}$	$\left[-1.7928\times10^{-9},\, -6.7798\times10^{-6},\, -8.8916\times10^{-9}\right]^{\mathrm{T}}$
6	$\left[5.6290\times10^{-7},\, -2.2537\times10^{-9},\, -1.8496\times10^{-6}\right]^{\mathrm{T}}$	$\left[1.7893\times10^{-9},\, 1.8775\times10^{-6},\, -8.9881\times10^{-9}\right]^{\mathrm{T}}$

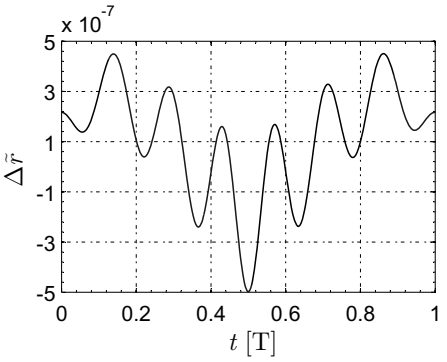

Figure 11: Dimensionless distance error of the 6th-order Fourier series-based approximation with respect to the numerical solution.

Table 2: Initial errors of three solar sails in the leaderless case.

	$\boldsymbol{e}_{ij_0}\cdot\hat{\boldsymbol{x}}$ [km]	$\boldsymbol{e}_{ij_0}\cdot\hat{\boldsymbol{y}}$ [km]	$\boldsymbol{e}_{ij_0}\cdot\hat{\boldsymbol{z}}$ [km]	$\dot{\boldsymbol{e}}_{ij_0}\cdot\hat{\boldsymbol{x}}$ [m/s]	$\dot{\boldsymbol{e}}_{ij_0}\cdot\hat{\boldsymbol{y}}$ [m/s]	$\dot{\boldsymbol{e}}_{ij_0}\cdot\hat{\boldsymbol{z}}$ [m/s]
$i=1,\, j=2$	1	2.5	-2	1×10^{-3}	-2×10^{-3}	2×10^{-3}
$i=2,\, j=3$	-2.5	-1.5	2.5	-1×10^{-3}	2×10^{-3}	-2×10^{-3}
$i=3,\, j=1$	1.5	-1	-0.5	-1×10^{-3}	1×10^{-3}	2×10^{-3}

The information exchange topology characterizing the mutual interaction of the three solar sails is assumed to follow a cyclic pursuit structure, as is illustrated in Fig. 12. In this case, the weighted adjacency matrix $\mathbb{W}$ is given by

$$\mathbb{W}=\begin{bmatrix} 0 & 8\times10^4 & 0 \\ 0 & 0 & 8\times10^4 \\ 8\times10^4 & 0 & 0 \end{bmatrix} \tag{63}$$

For a favorable control performance (in terms of convergence time and tracking accuracy), the dimensionless parameters in Eq. (40) are selected as $\alpha=2.5\times10^2$ and $\gamma=5\times10^{-3}$. Note that γ satisfies the constraint of Eq. (41), i.e. $\gamma>4.1\times10^{-3}$.

The position and velocity errors of the three solar sails are shown in Fig. 13 and Fig. 14 respectively, while the time variations of the (relative) control variables $\Delta\,\theta_i$, $\Delta\,\phi_i$ and $\Delta\,u_i$ are shown in Fig. 15.

Figure 16 illustrates the relative transfer trajectories of the three sails, whose initial positions are denoted with the star. It may be seen from the figures that with the control law (40), all errors converge to zero

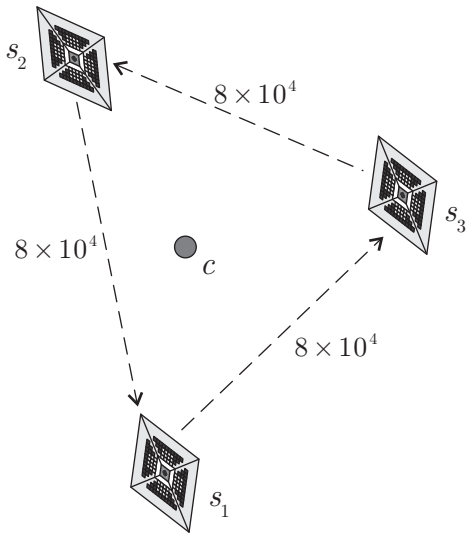

Figure 12: Information exchange topology of the three solar sails in the leaderless case.

within 1.5 days and a good synchronization is maintained along the whole maneuver. Moreover, the final consensus guarantees a similar transition time to all of the solar sails, which is a crucial point for practical applications.

6.2. Virtual-leader case

Consider now the case where a virtual leader v is included in the solar sail-based formation structure. The initial conditions of the three solar sails are slightly different from the desired trajectories, with the initial errors listed in Tab. 3. The location of the virtual leader has a small (constant) bias relative to the nominal trajectory. In the following examples, it is assumed that $[\boldsymbol{\rho}_v]_{\mathcal{T}} = [1,\, 0,\, 0]^{\mathrm{T}}$ km and $[\dot{\boldsymbol{\rho}}_v]_{\mathcal{T}} = \mathbf{0}_3$. In particular, illustrative examples will be discussed to verify the proposed control laws that account for the two previous subcases, where the virtual leader state is either accessible to all of the solar sails or to a subset of sails (that is, a part of the formation structure).

Table 3: Initial errors of three solar sails in the virtual-leader case.

	$\boldsymbol{e}_{x_0}$ [km]	$\boldsymbol{e}_{y_0}$ [km]	$\boldsymbol{e}_{z_0}$ [km]	$\dot{\boldsymbol{e}}_{x_0}$ [m/s]	$\dot{\boldsymbol{e}}_{y_0}$ [m/s]	$\dot{\boldsymbol{e}}_{z_0}$ [m/s]
s_1	1	-2.5	2	1×10^{-3}	-2×10^{-3}	2×10^{-3}
s_2	2.5	-2	-1	-1×10^{-3}	2×10^{-3}	-2×10^{-3}
s_3	-2.5	2	1	-1×10^{-3}	1×10^{-3}	2×10^{-3}

6.2.1. Full access to the virtual leader state

When all of the solar sails in formation have access to the data from the virtual leader v, the communication topology is illustrated in Fig. 17, where the information flows among the three spacecraft follow a cyclic pursuit pattern. In this case, the weighted adjacency matrix $\mathbb{W}$ is given by

$$\mathbb{W} = \begin{bmatrix} 0 & 1 & 0 \\ 0 & 0 & 1 \\ 1 & 0 & 0 \end{bmatrix} \tag{64}$$

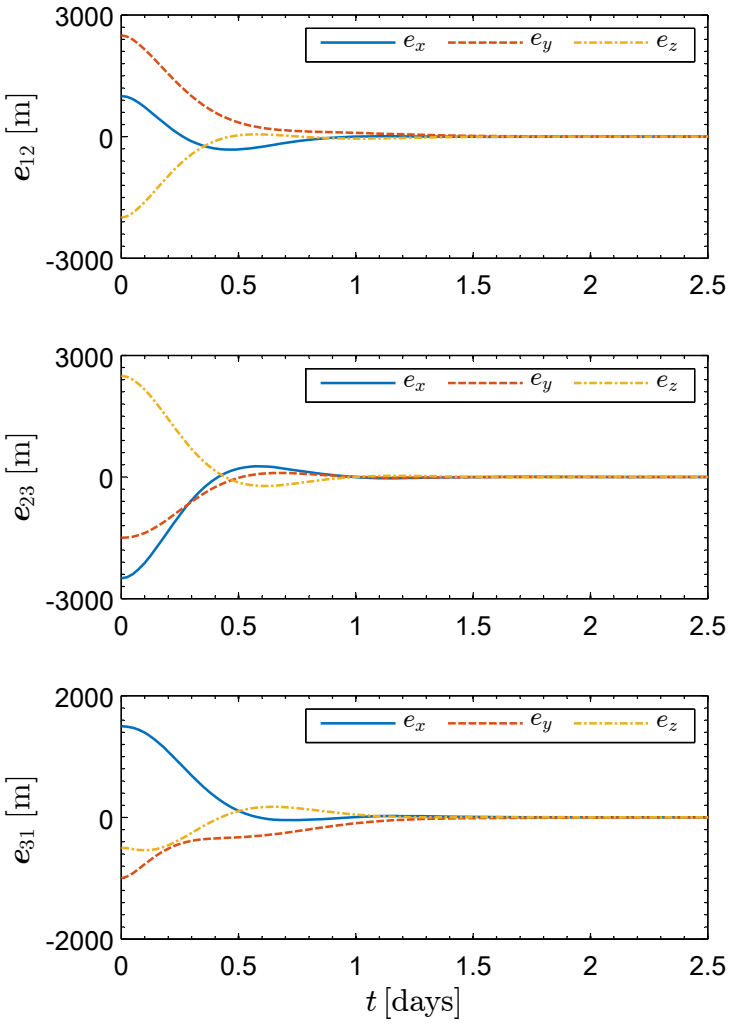

Figure 13: Time history of the position errors $\boldsymbol{e}_{ij}$ in a leaderless case.

The performance of the controller described by Eq. (52) is governed by the dimensionless parameters $\{\sigma, \zeta\}$, whose values are chosen as $\sigma = 10^5$ and $\zeta = 6.4 \times 10^{-3}$. Note that ζ satisfies the constraint of Eq. (53), i.e. $\zeta > 4.47 \times 10^{-3}$.

To illustrate the performance of the control law given by Eq. (52), the time variations of the relative position and velocity errors are plotted in Fig. 18 and Fig. 19, for a time interval of 2.5 days. The corresponding time histories of the required control variables $\Delta\,\theta_i$, $\Delta\,\phi_i$ and $\Delta\,u_i$ are shown in Fig. 20, while the relative trajectories of the three sails are illustrated in Fig. 21. It can be seen that the transient errors of the three solar sails gradually converge to zero after about 1.5 days.

6.2.2. Partial access to the virtual leader state

The control law given by Eq. (58) is now validated for the case in which the virtual leader state is available to only a part of the solar sail formation structure. Without loss of generality, only the solar sail s_1 is now assumed to have access to the virtual leader state, see Fig. 22. The initial errors take the same value as those reported in Tab. 3, and the weighted adjacent matrix is given by Eq. (64).

The parameters in Eq. (58) are selected as $\delta = 10^5$ and $\kappa = 7 \times 10^2$, and the weight of the directed edge between the virtual leader and the sail s_1 is $w_{10} = 1$. A first-order Eulerian differentiation method is adopted in the simulation, and the sampling interval is chosen to be $\tau = 5 \times 10^{-4}$ day.

The position and velocity errors of the three sails are illustrated in Fig. 23 and Fig. 24 respectively, while

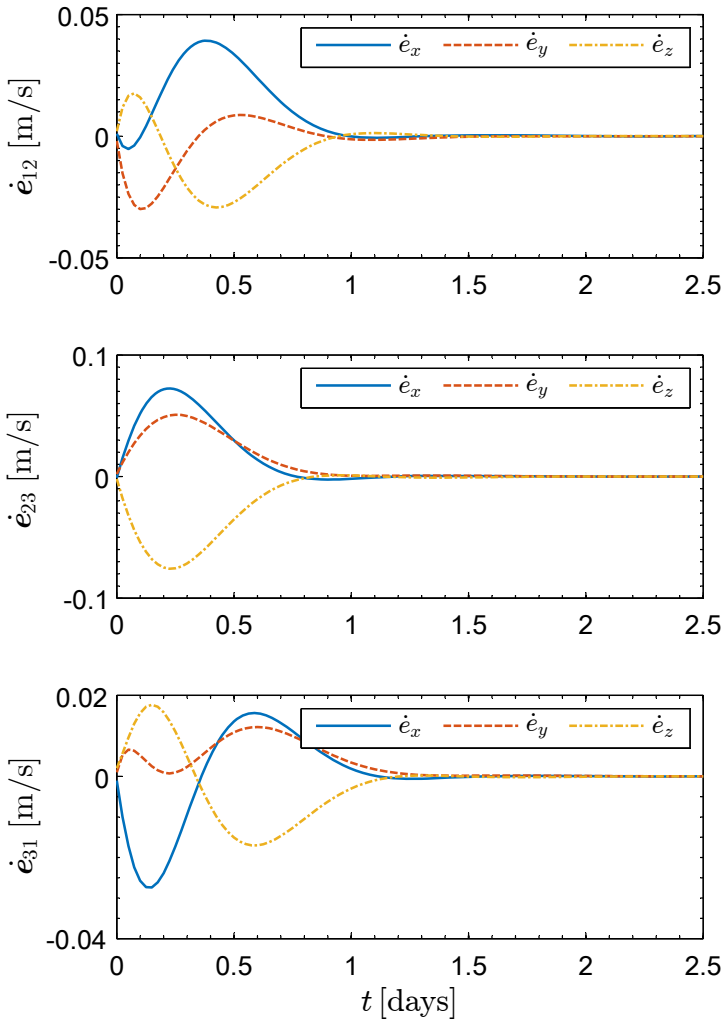

Figure 14: Time history of the velocity errors $\dot{\boldsymbol{e}}_{ij}$ in a leaderless case.

the control input $\boldsymbol{u}_i$ is shown in Fig. 25. The relative trajectories of the three sails are illustrated in Fig. 26. Note that, even in this case of partial access to the virtual leader state, the steady state errors of the three sails converge all to zero, while consensus is guaranteed during the whole transition phase.

The illustrative examples show that, to maintain a formation with a 10-km size, a propulsive acceleration with a magnitude of $0.05\,\mathrm{mm/s^2}$ is required for each solar sail. Such a performance level is achievable by current technology.

The previous theorems on the cooperative formation control do not take into account any constraint on the initial errors, which however significantly affect the magnitude of the control input $\Delta\,\boldsymbol{u}_i$. In particular, for a fixed set of control parameters, an actuator saturation may occur when the magnitude of the initial errors exceeds some maximum value (to be found by simulation). For this reason the choice of the control parameters is usually the output of a trial and error procedure. Nevertheless, some general remarks may simplify the design. For example, in the leaderless case it is preferable to choose a small value of γ in Eq. (40) to mitigate the saturation problem. In the virtual leader case, instead, the numerical simulations suggest to decrease ζ in Eq. (52) and decrease κ in Eq. (58), when a saturation of control input occurs.

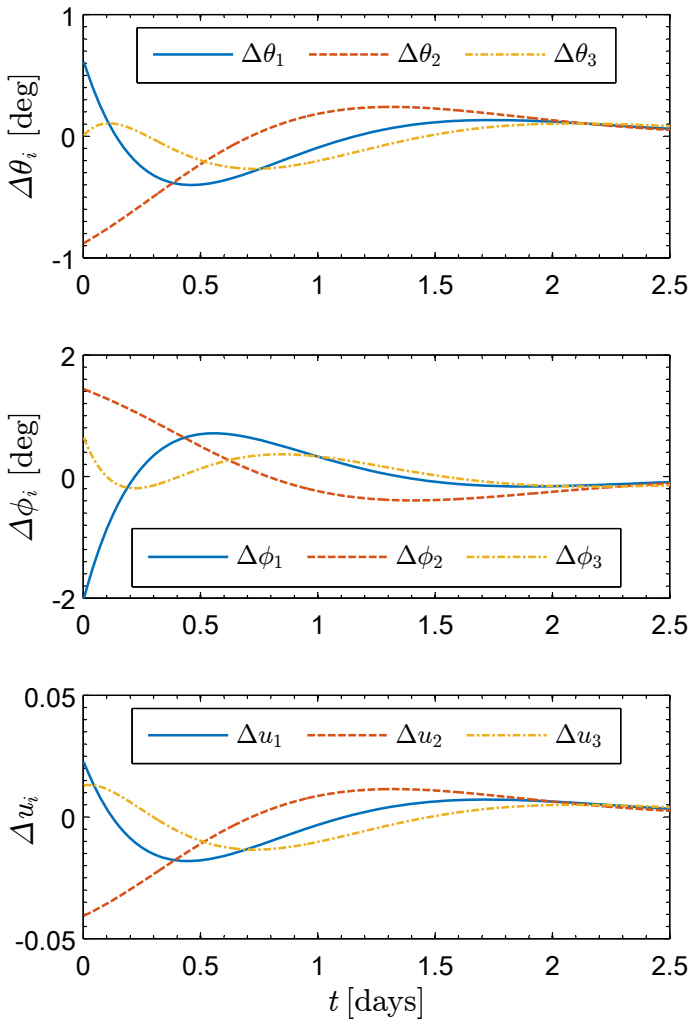

Figure 15: Time history of the control input $\Delta \boldsymbol{u}_i$ of the three solar sails, see Eq. (40).

7. Conclusions

The problem of solar sail cooperative formation flying around L_2-type artificial Equilibrium point orbits in the Sun-[Earth+Moon] system has been investigated. A truncated Fourier series has been used to parameterize the artificial halo orbit in an explicit (albeit approximate) form, which is used as a nominal trajectory for the solar sail-based formation. Distributed control strategies have been proposed to account for two typical cases, according to whether the formation system is leaderless or accommodates a virtual leader. The latter case has been further discussed when the state information of the virtual leader is available to all of the solar sails or to a part of the formation structure only.

The constitution and maintenance of the solar sail-based formation relies on the consensus protocols that are formulated on a general directed communication topology with local neighbor-to-neighbor information networks. Such a cooperative formation structure drives each solar sail toward a desired trajectory in a coordinate way, so that the synchronized formation tracking can be achieved while improving the formation reliability.

Illustrative examples have shown that the proposed consensus-based algorithms also guarantee a time-balanced maneuver. Compared with a leader-follower topological structure, more flexility and robustness among the formation is incorporated both for the leaderless and the virtual-leader case, in the sense that onboard sensors with a limited field of view can be implemented, and data package loss for some interaction

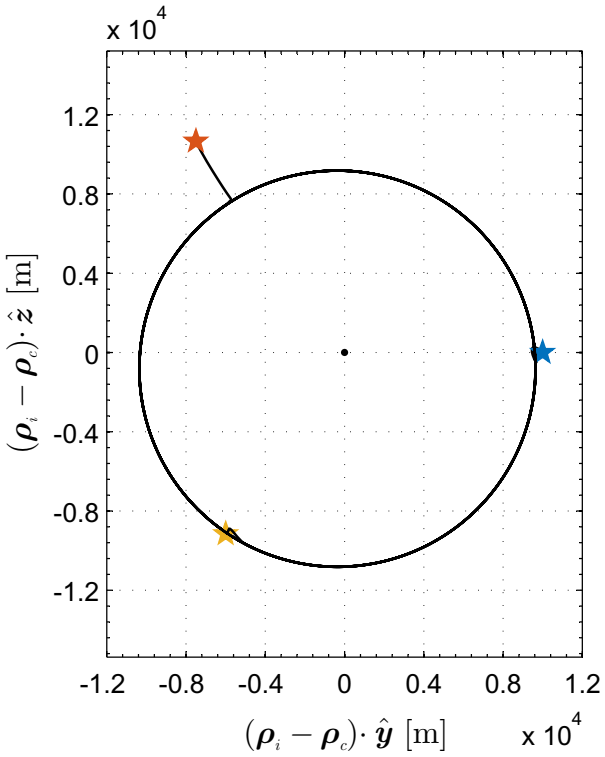

Figure 16: Relative trajectories of the three solar sails in a leaderless case (star denotes initial position).

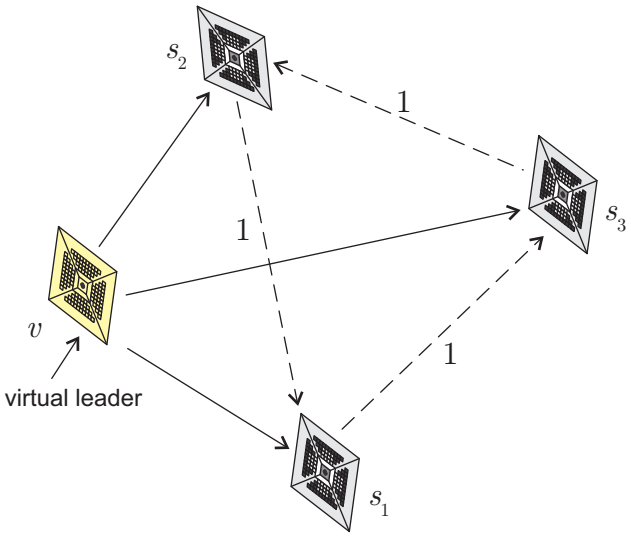

Figure 17: Information exchange topology where all the sails have access to the virtual leader.

links can be accounted for.

A natural extension of this work is the study of smart dust-based formation flying around a conventional spacecraft (a sort of mother-ship), which covers a halo orbit around the two collinear Lagrangian points near the [Earth+Moon] system. In that case, however, the small capability of those spacecraft to modulate the thrust vector and communicate with the neighbouring spacecraft, poses challenging constraints on the design of a cooperative control law.

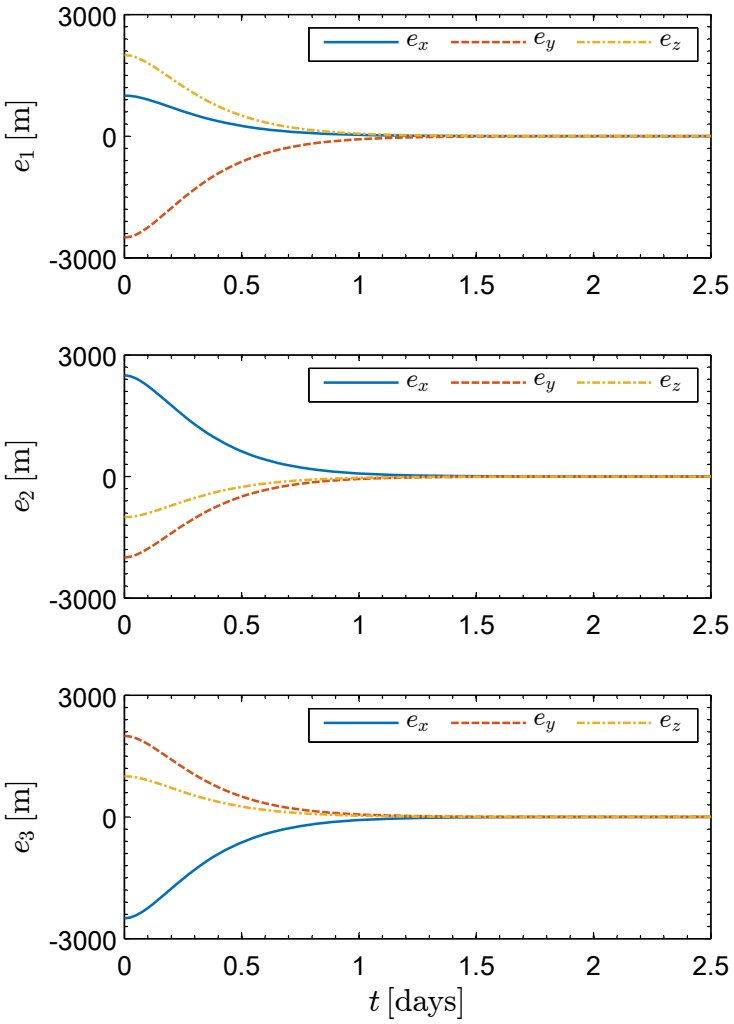

Figure 18: Time history of the position errors $\boldsymbol{e}_i$ when all of the sails have access to the virtual leader.

Acknowledgements

This work was supported by the National Science Fund for Distinguished Young Scholars of China (Grant no. 11525208) and University of Pisa, Progetti di Ricerca di Ateneo (Grant no. PRA_2018_44).

References

[1] Q. Wang, J. Liu, A Chang'e-4 mission concept and vision of future Chinese lunar exploration activities, Acta Astronautica 127 (2016) 678–683, doi: 10.1016/j.actaastro.2016.06.024.

[2] J. Heiligers, B. Diedrich, W. Derbes, C. McInnes, Sunjammer: preliminary end-to-end mission design, in: AIAA/AAS Astrodynamics Specialist Conference, San Diego, CA, USA, 2014, AIAA Paper 2014-4127.

[3] J. Heiligers, J. Parker, M. Macdonald, Novel solar-sail mission concepts for high-latitude Earth and lunar observation, Journal of Guidance, Control, and Dynamics 41 (1) (2018) 212–230, doi: 10.2514/1.G002919.

[4] M. T. Ozimek, D. J. Grebow, K. C. Howell, Design of solar sail trajectories with applications to lunar south pole coverage, Journal of Guidance, Control, and Dynamics 32 (6) (2009) 1884–1897, doi: 10.2514/1.41963.

[5] C. R. McInnes, Solar sail trajectories at the lunar L_2 lagrange point, Journal of Spacecraft and Rockets 30 (6) (1993) 782–784, doi: 10.2514/3.26393.

[6] Y. Jia, Y. Zou, J. Ping, C. Xue, J. Yan, Y. Ning, The scientific objectives and payloads of Chang'E-4 mission, Planetary and Space Science 162 (2018) 207–215, doi: 10.1016/j.pss.2018.02.011.

[7] V. Domingo, B. Fleck, A. I. Poland, The SOHO mission: an overview, Solar Physics 162 (1–2) (1995) 1–37, doi: 10.1007/BF00733425.

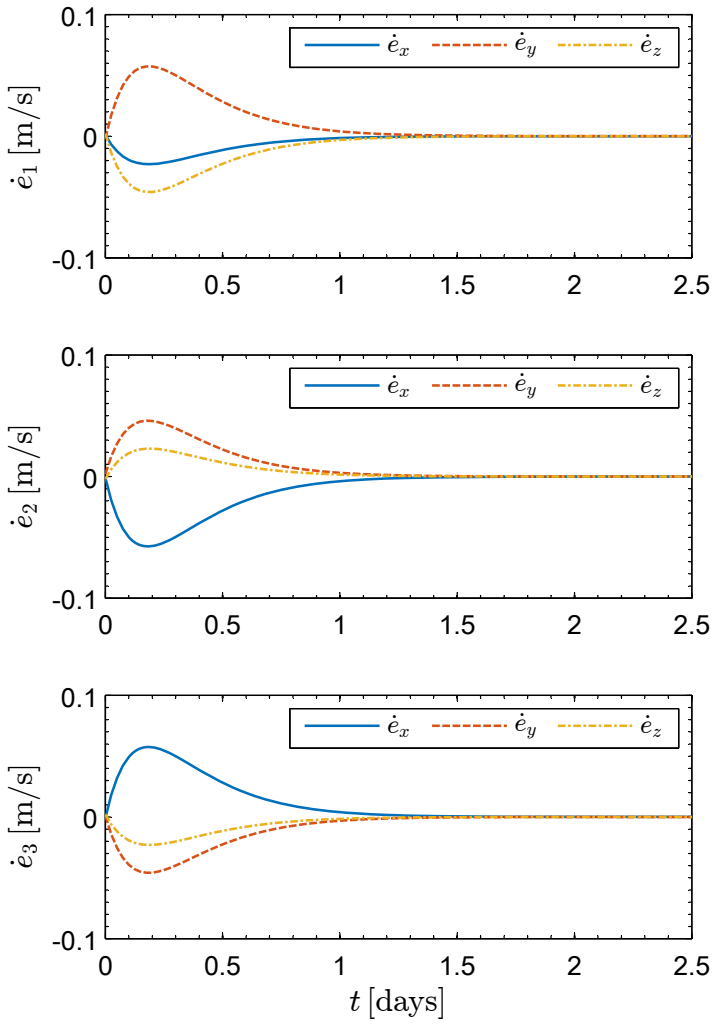

Figure 19: Time history of the velocity errors $\dot{\boldsymbol{e}}_i$ when all of the sails have access to the virtual leader.

[8] J. Burt, B. Smith, Deep space climate observatory: The DSCOVR mission, in: 2012 IEEE Aerospace Conference, Big Sky, MT, USA, 2012, pp. 1–13.

[9] S. Edberg, W. Traub, S. Unwin, J. Marr IV, The SIM PlanetQuest science program, Acta Astronautica 61 (1-6) (2007) 52–62, doi: 10.1016/j.actaastro.2007.01.036.

[10] M. Hechler, M. Mora, M. Sanchez Nogales, A. Yanez, Orbit concepts at L_2 for Soyuz launches from Kourou, Acta Astronautica 62 (2-3) (2008) 140–150, doi: 10.1016/j.actaastro.2006.12.036.

[11] C. Colombo, E. Alessi, W. Weg, S. Soldini, F. Letizia, M. Vetrisano, M. Vasile, A. Rossi, M. Landgraf, End-of-life disposal concepts for libration point orbit and highly elliptical orbit missions, Acta Astronautica 110 (2015) 298–312, doi: 10.1016/j.actaastro.2014.11.002.

[12] M. Landgraf, F. Renk, B. De Vogeleer, Mission design and analysis of European astrophysics missions orbiting libration points, Acta Astronautica 84 (2013) 49–55, doi: 10.1016/j.actaastro.2012.10.005.

[13] U. Feucht, G. Gienger, Launch and early operations of Herschel and Planck, Acta Astronautica 68 (7-8) (2011) 1283–1291, doi: 10.1016/j.actaastro.2010.09.003.

[14] J.-M. Reix, T. Passvogel, G. Crone, B. Collaudin, P. Rideau, Y. Roche, C. Vogel, The Herschel/Planck programme, technical challenges for two science missions, successfully launched, Acta Astronautica 66 (1-2) (2010) 130–148, doi: 10.1016/j.actaastro.2009.05.025.

[15] M. Hechler, Launch windows for libration point missions, Acta Astronautica 64 (2-3) (2009) 139–151, doi: 10.1016/j.actaastro.2008.07.013.

[16] C. Maccone, M. Gai, The data compression problem for the 'GAIA' astrometric satellite of ESA, Acta Astronautica 44 (7) (1999) 375–384, doi: 10.1016/S0094-5765(99)00077-6.

[17] R. Keil, D. Risquez, F. Van Leeuwen, A. Brown, An attitude model for the spacecraft of the ESA mission Gaia, Acta Astronautica 69 (9-10) (2011) 869–881, doi: 10.1016/j.actaastro.2011.04.021.

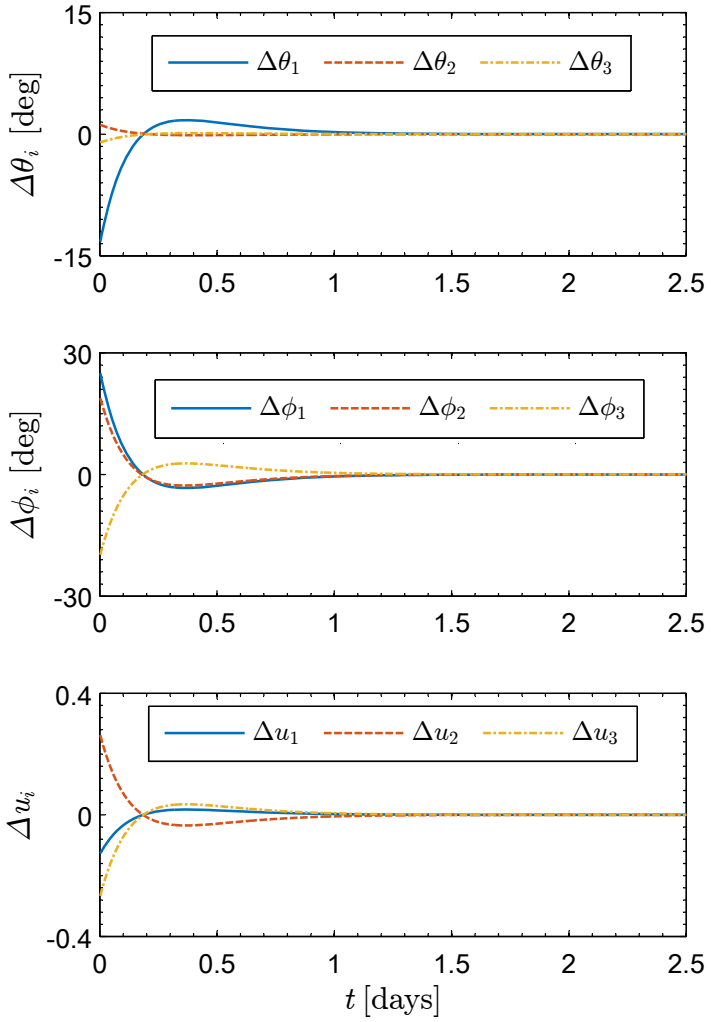

Figure 20: Time history of the control input $\Delta \boldsymbol{u}_i$ of the three sails, see Eq. (52).

[18] D. Milligan, A. Rudolph, G. Whitehead, T. Loureiro, E. Serpell, F. Di Marco, J. Marie, E. Ecale, ESA's billion star surveyor - Flight operations experience from Gaia's first 1.5 years, Acta Astronautica 127 (2016) 394–403, doi: 10.1016/j.actaastro.2016.06.026.

[19] E. Wille, M. Bavdaz, European X-ray optics for next generation space observatories, Acta Astronautica 116 (2015) 50–55, doi: 10.1016/j.actaastro.2015.06.011.

[20] P. De Korte, Technology developments needed for future X-ray astronomy missions, Acta Astronautica 77 (2012) 118–125, doi: 10.1016/j.actaastro.2012.03.015.

[21] R. Ragazzoni, H. Rauer, C. Catala, et al., A one meter class eye for the planetary transit and oscillation spacecraft, Acta Astronautica 115 (2015) 18–23, doi: 10.1016/j.actaastro.2015.04.026.

[22] M. Shirobokov, S. Trofimov, M. Ovchinnikov, Survey of station-keeping techniques for libration point orbits, Journal of Guidance, Control, and Dynamics 40 (5) (2017) 1085–1105, doi: 10.2514/1.G001850.

[23] J. Heiligers, S. Hiddink, R. Noomen, C. McInnes, Solar sail Lyapunov and halo orbits in the Earth-Moon three-body problem, Acta Astronautica 116 (2015) 25–35, doi: 10.1016/j.actaastro.2015.05.034.

[24] H. Baoyin, C. R. McInnes, Solar sail halo orbits at the Sun-Earth artificial L_1 point, Celestial Mechanics and Dynamical Astronomy 94 (2) (2006) 155–171, doi: 10.1007/s10569-005-4626-3.

[25] A. Farrés, A. Jorba, Dynamics of a solar sail near a halo orbit, Acta Astronautica 67 (7-8) (2010) 979–990, doi: 10.1016/j.actaastro.2010.05.022.

[26] J. Heiligers, M. Macdonald, J. S. Parker, Extension of Earth-Moon libration point orbits with solar sail propulsion, Astrophysics and Space Science 361 (241), doi: 10.1007/s10509-016-2783-3.

[27] P. Verrier, T. Waters, J. Sieber, Evolution of the L_1 halo family in the radial solar sail circular restricted three-body problem, Celestial Mechanics and Dynamical Astronomy 120 (4) (2014) 373–400, doi: 10.1007/s10569-014-9575-2.

[28] Y. Tsuda, O. Mori, R. Funase, H. Sawada, T. Yamamoto, T. Saiki, T. Endo, J. Kawaguchi, Flight status of IKAROS deep

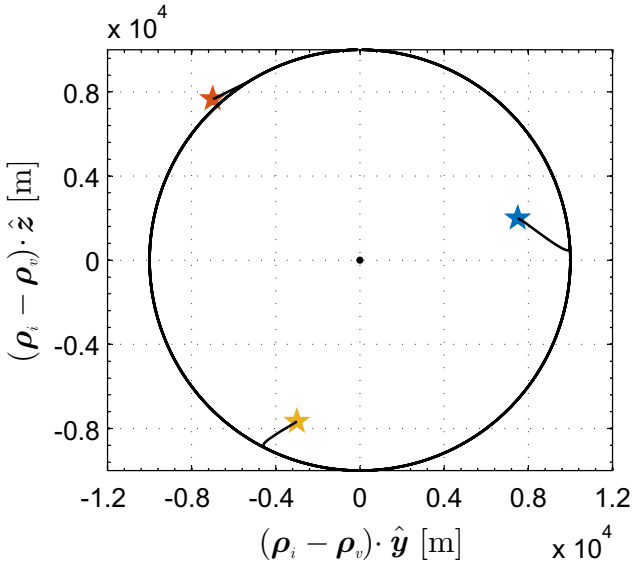

Figure 21: Relative trajectories of the three sails when all of the sails have access to the virtual leader.

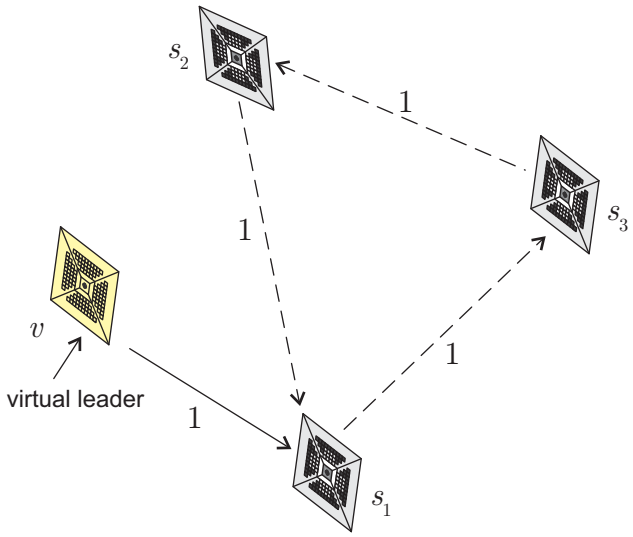

Figure 22: Information exchange topology where only a part of the formation have access to the virtual leader.

space solar sail demonstrator, Acta Astronautica 69 (9-10) (2011) 833–840, doi: 10.1016/j.actaastro.2011.06.005.

[29] Y. Tsuda, O. Mori, R. Funase, H. Sawada, T. Yamamoto, T. Saiki, T. Endo, K. Yonekura, H. Hoshino, J. Kawaguchi, Achievement of IKAROS–Japanese deep space solar sail demonstration mission, Acta Astronautica 82 (2) (2013) 183–188, doi: 10.1016/j.actaastro.2012.03.032.

[30] L. Johnson, M. Whorton, A. Heaton, R. Pinson, G. Laue, C. Adams, NanoSail-D: A solar sail demonstration mission, Acta Astronautica 68 (5-6) (2011) 571–575, doi: 10.1016/j.actaastro.2010.02.008.

[31] L. Johnson, R. Young, E. Montgomery, D. Alhorn, Status of solar sail technology within NASA, Advances in Space Research 48 (11) (2011) 1687–1694, doi: 10.1016/j.asr.2010.12.011.

[32] P. Janhunen, Electric sail for spacecraft propulsion, Journal of Propulsion and Power 20 (4) (2004) 763–764, doi: 10.2514/1.8580.

[33] P. Janhunen, A. A. Quarta, G. Mengali, Electric solar wind sail mass budget model, Geoscientific Instrumentation, Methods and Data Systems 2 (1) (2013) 85–95, doi: 10.5194/gi-2-85-2013.

[34] C. R. McInnes, Solar Sailing: Technology, Dynamics and Mission Applications, Springer-Praxis Series in Space Science and Technology, Springer-Verlag, Berlin, 1999.

[35] W. Wang, J. Yuan, G. Mengali, A. A. Quarta, Invariant manifold and bounds of relative motion between heliocentric

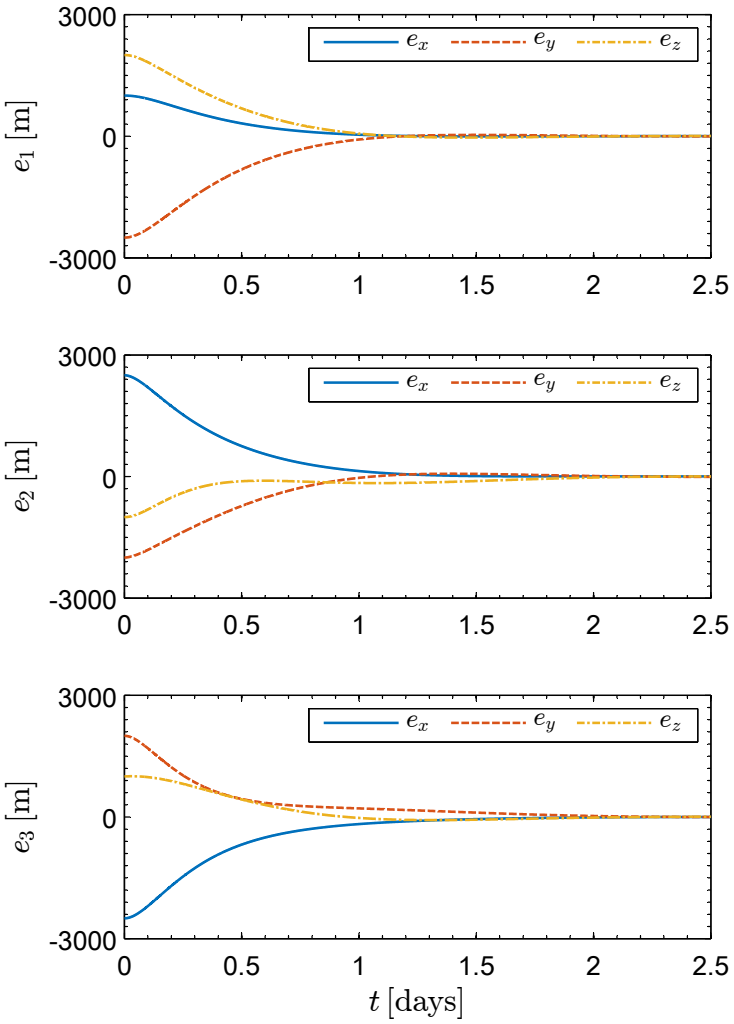

Figure 23: Time history of the position errors $\boldsymbol{e}_i$ when the sail s_1 only has access to the virtual leader.

displaced orbits, Journal of Guidance, Control and Dynamics 39 (8) (2016) 1764–1776, doi: 10.2514/1.G001751.

[36] S. Gong, H. Baoyin, J. Li, Solar sail formation flying around displaced solar orbits, Journal of Guidance, Control, and Dynamics 30 (4) (2007) 1148–1152, doi: 10.2514/1.24315.

[37] J. D. Biggs, C. R. McInnes, Solar sail formation flying for deep-space remote sensing, Journal of Spacecraft and Rockets 46 (3) (2009) 670–678, doi: 10.2514/1.42404.

[38] K. Parsay, H. Schaub, Designing solar sail formations in sun-synchronous orbits for geomagnetic tail exploration, Acta Astronautica 107 (2015) 218–233, doi: 10.1016/j.actaastro.2014.11.018.

[39] S. Bandyopadhyay, R. Foust, G. P. Subramanian, S.-J. Chung, F. Y. Hadaegh, Review of formation flying and constellation missions using nanosatellites, Journal of Spacecraft and Rockets 53 (3) (2016) 567–578, doi: 10.2514/1.A33291.

[40] W. Wang, G. Mengali, A. A. Quarta, J. Yuan, Multiple solar sail formation flying around heliocentric displaced orbit via consensus, Acta Astronautica 154 (2019) 256–267, doi: 10.1016/j.actaastro.2018.03.039.

[41] R. W. Beard, J. Lawton, F. Y. Hadaegh, A coordination architecture for spacecraft formation control, IEEE Transactions on control systems technology 9 (6) (2001) 777–790, doi: 10.1109/87.960341.

[42] W. Ren, R. W. Beard, Formation feedback control for multiple spacecraft via virtual structures, IEE Proceedings-Control Theory and Applications 151 (3) (2004) 357–368, doi: 10.1049/ip-cta:20040484.

[43] W. Ren, Formation keeping and attitude alignment for multiple spacecraft through local interactions, Journal of Guidance, Control, and Dynamics 30 (2) (2007) 633–638, doi: 10.2514/1.25629.

[44] W. Wang, G. Mengali, A. A. Quarta, J. Yuan, Formation flying for electric sails in displaced orbits. Part I: Geometrical analysis, Advances in Space Research 60 (6) (2017) 1115–1129, doi: 10.1016/j.asr.2017.05.015.

[45] W. Wang, G. Mengali, A. A. Quarta, J. Yuan, Formation flying for electric sails in displaced orbits. Part II: Distributed coordinated control, Advances in Space Research 60 (6) (2017) 1130–1147, doi: 10.1016/j.asr.2017.06.017.

[46] T. Chen, H. Wen, H. Hu, D. Jin, Output consensus and collision avoidance of a team of flexible spacecraft for on-orbit

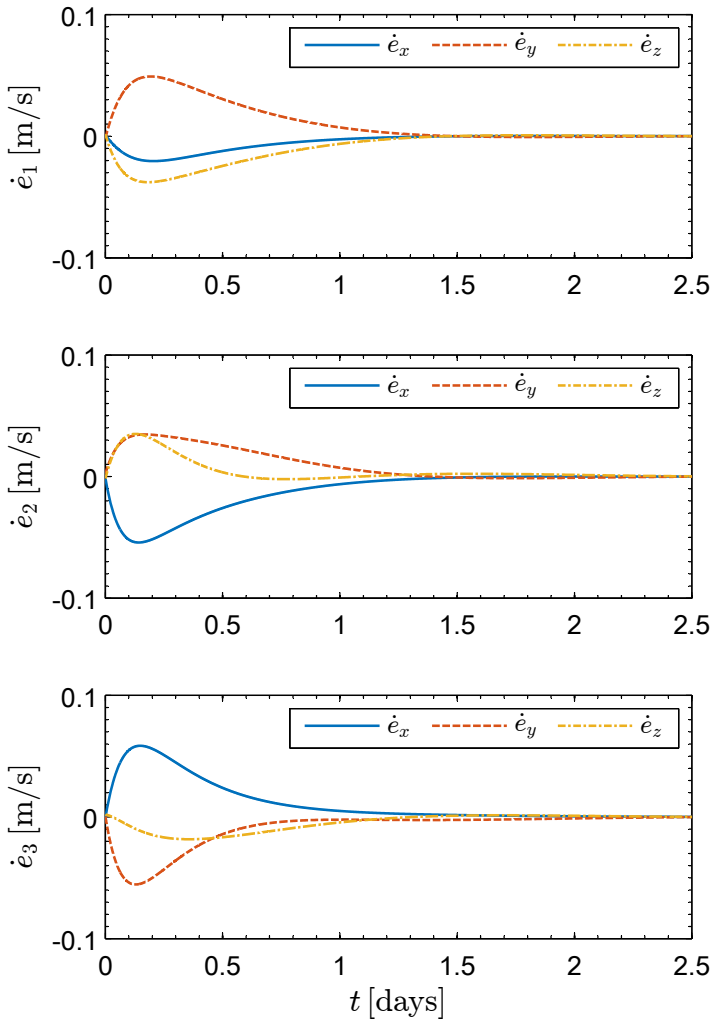

Figure 24: Time history of the velocity errors $\dot{\boldsymbol{e}}_i$ when the sail s_1 only has access to the virtual leader.

autonomous assembly, Acta Astronautica 121 (2016) 271–281, doi: 10.1016/j.actaastro.2015.11.004.

[47] B. Zhang, S. Song, Decentralized coordinated control for multiple spacecraft formation maneuvers, Acta Astronautica 74 (2012) 79–97, doi: 10.1016/j.actaastro.2011.12.017.

[48] B. Cong, X. Liu, Z. Chen, Distributed attitude synchronization of formation flying via consensus-based virtual structure, Acta Astronautica 68 (11-12) (2011) 1973–1986, doi: 10.1016/j.actaastro.2010.11.014.

[49] J. L. Wright, Space Sailing, Gordon and Breach Science Publishers , 1992, pp. 223–233.

[50] J. Mu, S. Gong, J. Li, Reflectivity-controlled solar sail formation flying for magnetosphere mission, Aerospace Science and Technology 30 (1) (2013) 339–348, doi: 10.1016/j.ast.2013.09.002.

[51] F. J. T. Salazar, C. R. McInnes, O. C. Winter, Periodic orbits for space-based reflectors in the circular restricted three-body problem, Celestial Mechanics and Dynamical Astronomy 128 (1) (2017) 95–113, doi: 10.1007/s10569-016-9739-3.

[52] C. R. McInnes, Orbits in a generalized two-body problem, Journal of Guidance, Control, and Dynamics 26 (5) (2003) 743–749, doi: 10.2514/2.5129.

[53] G. Mengali, A. A. Quarta, Optimal control laws for axially symmetric solar sails, Journal of Spacecraft and Rockets 42 (6) (2005) 1130–1133, doi: 10.2514/1.17102.

[54] C. Colombo, C. Lücking, C. R. McInnes, Orbit evolution, maintenance and disposal of spacechip swarms through electrochromic control, Acta Astronautica 82 (1) (2013) 25–37, doi: 10.1016/j.actaastro.2012.05.035.

[55] C. Colombo, C. R. McInnes, Orbit design for future spacechip swarm missions in a planetary atmosphere, Acta Astronautica 75 (2012) 25–41, doi: 10.1016/j.actaastro.2012.01.004.

[56] A. A. Quarta, G. Mengali, E. Denti, Optimal in-orbit repositioning of sun-pointing smart dust, Acta Astronautica 154 (2019) 278–285, doi: 10.1016/j.actaastro.2018.03.036.

[57] L. Niccolai, M. Bassetto, A. A. Quarta, G. Mengali, A review of smart dust architecture, dynamics, and mission applications, Progress in Aerospace Sciences 106 (2019) 1–14, doi: 10.1016/j.paerosci.2019.01.003.

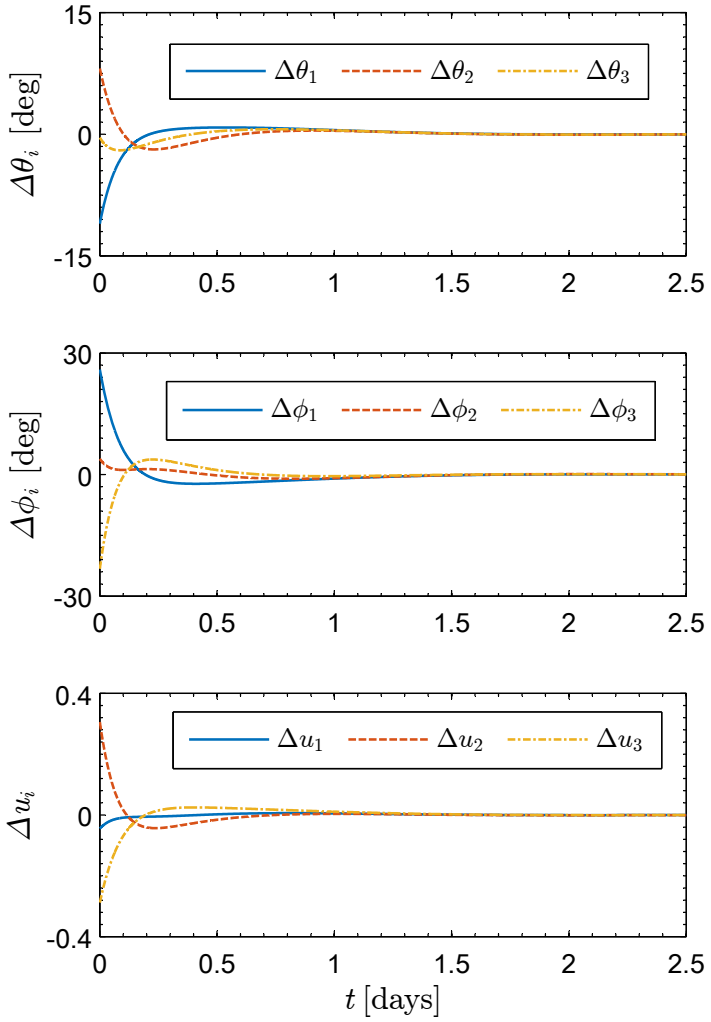

Figure 25: Time history of the control input $\Delta \boldsymbol{u}_i$ of the three sails when only s_1 has access to the virtual leader.

[58] J. A. Atchison, M. A. Peck, A passive, sun-pointing, millimeter-scale solar sail, Acta Astronautica 67 (1-2) (2010) 108–121, doi: 10.1016/j.actaastro.2009.12.008.

[59] K. Shahid, K. D. Kumar, Formation control at the Sun-Earth L_2 libration point using solar radiation pressure, Journal of Guidance, Control, and Dynamics 47 (4) (2010) 614–626, doi: 10.2514/1.47342.

[60] A. I. S. McInnes, Strategies for solar sail mission design in the circular restricted three-body problem, MSE Thesis, School of Aeronautics and Astronautics, Purdue University (2000) 472–479 .

[61] K. C. Howell, Three-dimensional, periodic, 'halo' orbits, Celestial mechanics 32 (1) (1984) 53–71, doi: 10.1007/BF01358403.

[62] T. J. Waters, C. R. Mcinnes, Periodic orbits above the ecliptic in the solar-sail restricted three-body problem, Journal of Guidance, Control, and Dynamics 30 (3) (2007) 687–693, doi: 10.2514/1.26232.

[63] W. Wang, G. Mengali, A. A. Quarta, J. Yuan, Distributed adaptive synchronization for multiple spacecraft formation flying around lagrange point orbits, Aerospace Science and Technology 74 (2018) 93–103, doi: 10.1016/j.ast.2018.01.007.

[64] W. Ren, Multi-vehicle consensus with a time-varying reference state, System & Control Letters 56 (7–8) (2007) 474–483, doi: 10.1016/j.sysconle.2007.01.002.

[65] W. Ren, E. Atkins, Distributed multi-vehicle coordinated control via local information exchange, International Journal of Robust and Nonlinear Control 17 (11) (2007) 1002–1033, doi: 10.1002/rnc.1147.

[66] D. Spielman, Spectral Graph Theory, Chapman and Hall/CRC, 2012, Ch. 18, pp. 495–500.

[67] T. Balch, R. C. Arkin, Behavior-based formation control for multirobot teams, IEEE Transactions on Robotics and Automation 14 (6) (1998) 926–939, doi: 10.1002/rnc.1147.

[68] H. Zhang, P. Gurfil, Distributed control for satellite cluster flight under different communication topologies, Journal of Guidance, Control, and Dynamics 39 (3) (2016) 617–627, doi: 10.2514/1.G001355.

[69] D. Thakur, S. Hernandez, M. R. Akella, Spacecraft swarm finite-thrust cooperative control for common orbit convergence, Journal of Guidance, Control, and Dynamics 38 (3) (2015) 478–488, doi: 10.2514/1.G000621.

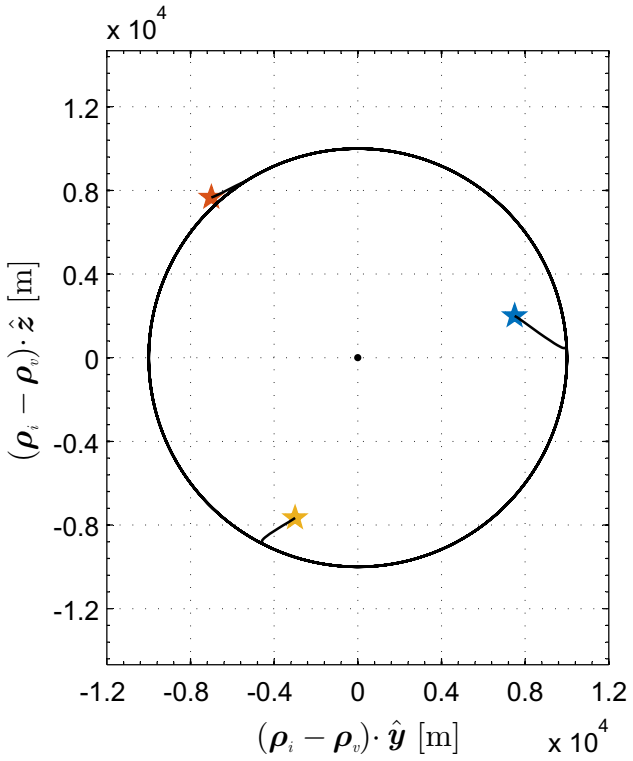

Figure 26: Relative trajectories of the three sails when the sail s_1 only has access to the virtual leader.

[70] G. Liu, S. Zhang, A survey on formation control of small satellites, Proceedings of the IEEE 106 (3) (2018) 440–457, doi: 10.1109/JPROC.2018.2794879.

[71] W. Ren, R. W. Beard, Decentralized scheme for spacecraft formation flying via the virtual structure approach, Journal of Guidance, Control, and Dynamics 27 (1) (2004) 73–82, doi: 10.2514/1.9287.